

Decomposing observations of high-frequency radar-derived surface currents by their forcing mechanisms: Locally wind-driven surface currents

Sung Yong Kim,¹ Bruce D. Cornuelle,² and Eric J. Terrill¹

Received 22 February 2010; revised 20 September 2010; accepted 30 September 2010; published 18 December 2010.

[1] The wind impulse response function and transfer function for high-frequency radar-derived surface currents off southern San Diego are calculated using several local wind observations. The spatial map of the transfer function reflects the influence of the coast on wind-current dynamics. Near the coast (within 20 km from the shoreline), the amplitudes of the transfer function at inertial and diurnal frequencies are reduced due to effects of coastline and bottom bathymetry. Meanwhile, the amplitude of low-frequency currents increases near the coast, which is attributed to the local geostrophic balance between cross-shore pressure gradients against the coast and currents. Locally wind-driven surface currents are estimated from the data-derived response function, and their power spectrum shows a strong diurnal peak superposed on a red spectrum, similar to the spectra of observed winds. Current magnitudes and veering angles to a quasi-steady wind are typically 2–5% of the wind speed and vary 50°–90° to the right of the wind, respectively. A wind skill map is introduced to present the fractional variance of surface currents explained by local winds as a verification tool for wind data quality and relevance. Moreover, the transfer functions in summer and winter are presented to examine the seasonal variation in ocean surface current response to the wind associated with stratification change.

Citation: Kim, S. Y., B. D. Cornuelle, and E. J. Terrill (2010), Decomposing observations of high-frequency radar-derived surface currents by their forcing mechanisms: Locally wind-driven surface currents, *J. Geophys. Res.*, 115, C12046, doi:10.1029/2010JC006223.

1. Introduction

[2] Surface currents driven by local winds are classified into two kinds of currents by the nature of the mechanical coupling: wind-drift currents accelerated directly by wind friction (called wind-driven surface currents herein) and wave-drift currents (Stokes drift) induced by nonlinearity of surface waves.

[3] Wind-driven currents at the surface may be in the wall layer or inertial sublayer, which is a logarithmic boundary layer ($O(1)$ m) between the air-sea interface and the top of the Ekman layer. The veering angles of wind-driven currents within the wall layer range from zero to 45° to the right of the wind direction (northern hemisphere), and their magnitudes are 2–3% of the wind speed [e.g., Ekman, 1905; Bye, 1965; Madsen, 1977; Csanady, 1982; Fernandez et al., 1996; Almeida, 2008]. In statistical analyses of the wind and currents, the locally wind-driven currents have been

parameterized by the wind velocity or wind stress using linear and nonlinear models [e.g., Prandle, 1987; Essen, 1993; Ng, 1993; Rabinovich et al., 2007]. On the other hand, the wind impulse response function between wind stress and currents has been studied for theoretical interpretation [e.g., Ekman, 1905; Gonella, 1972; Weller, 1981; Rio and Hernandez, 2003; Elipot, 2006; Kim et al., 2009]. In addition, the surface layer jet within the mixed layer depends on the heat flux and surface wind stress [e.g., Phillips, 1966; Price et al., 1986], and seasonal and daily stratification changes can induce 1–3 cm s⁻¹ and larger currents [e.g., Graber et al., 1997; Cronin and Kessler, 2008].

[4] As an additional form of wind-driven ocean responses, the momentum transferred from the wind into the ocean generates ocean waves, and their nonlinear character causes Stokes drift. In general, Stokes drift depends on both wavelength and amplitude of surface waves, i.e., wave steepness, and decays exponentially in depth [e.g., Kenyon, 1969; Essen, 1993]. It was reported as 7–14 cm s⁻¹ at the surface and ~2 cm s⁻¹ at 1 m depth under wind speeds of 5–10 m s⁻¹ [e.g., Graber et al., 1997; Laws, 2001; Ullman et al., 2006]. Ullman et al. [2006] and Mao and Heron [2008] have investigated that the high-frequency radar (HFR) current measurements can contain the Stokes drift

¹Marine Physical Laboratory, Scripps Institution of Oceanography, University of California, San Diego, La Jolla, California, USA.

²Climate, Atmospheric Science and Physical Oceanography, Scripps Institution of Oceanography, University of California, San Diego, La Jolla, California, USA.

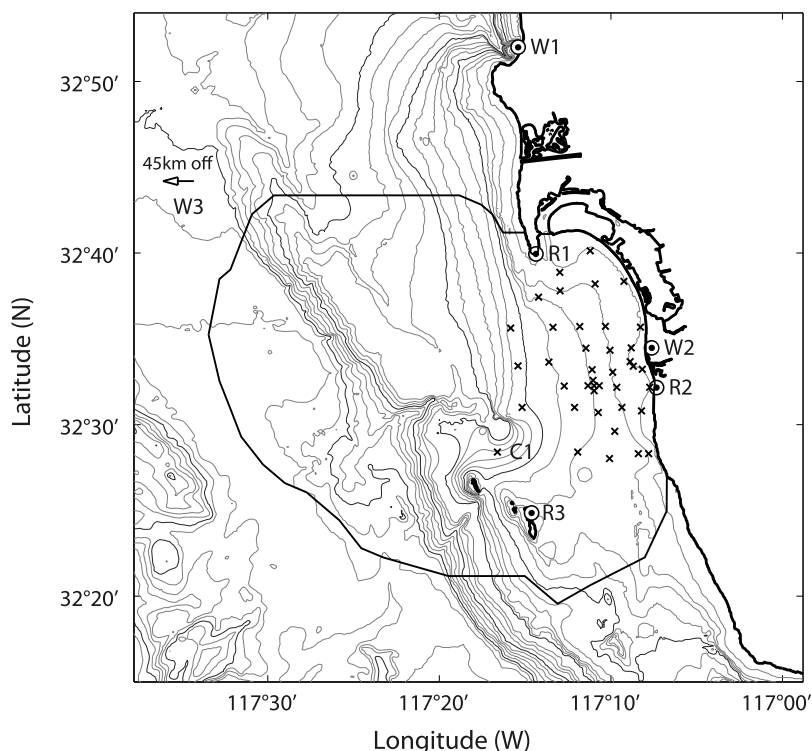


Figure 1. A study domain for investigation of the transfer function between surface currents and local winds and its spatial structure and seasonal characteristics. Three HFRs for surface current observations (Point Loma (SDPL, R1), Border Park (SDBP, R2), and Coronado Islands (SDCI, R3)), two shore stations (Scripps Pier (SIO, W1) and Tijuana River (TJR, W2)), one offshore buoy (NDBC, W3; 45 km west of the northwest edge of the domain) for winds, and 40 stations for CTD cast (cross marks, C1 station is a representative location) are indicated. A black outline denotes the effective coverage area of HFRs (at least 70% data availability for 2 years). The bottom bathymetry contours are indicated by thin curves with 10 m ($0 < z < 100$ m) and 50 m ($100 < z < 1000$ m) contour intervals and thick curves at the 50, 100, 500, and 1000 m depths.

using drifter tracks and the wind-current model under different fetch conditions, respectively. However, as the order of magnitude of the Stokes drift in this study area would be less than the uncertainty of the HFR measurements, the Stokes drift may not be clearly resolved by the statistical analysis (see Appendix A for more details).

[5] The high-resolution surface current maps (hourly in time and km in space) using HFRs allow us to examine the detailed surface circulation in the coastal region. Especially, wind-driven circulation correlated with local wind observations can be easily documented such as coastal boundary effects and ocean responses at diurnal and inertial frequencies. The locally wind-driven surface currents off southern San Diego is one of dominant current components, explaining approximately 30% of variance in total surface currents [e.g., Kim *et al.*, 2010]. The physical interpretation of the transfer function derived from regionally averaged surface currents and a single local wind observation off southern San Diego has been done elsewhere [e.g., Kim *et al.*, 2009]. Therefore we examine the spatial structure of transfer functions (section 4.1) using multiple wind observations and introduce a wind skill map (section 4.2), then describe their differences in summer and winter (section 4.4). The labels “summer” and “winter”

hereafter are referred to as April–September and October–March, respectively.

2. Summary of Observations

[6] The surface current response to local winds are estimated using HFR surface currents and winds observed at two local shore-based stations (Scripps Pier (SIO) and Tijuana River (TJR)) and one offshore buoy (National Data Buoy Center (NDBC) 46086, 85 km from coast, herein denoted NDBC) (Figure 1). The stratification in summer and winter is computed from monthly conductivity-temperature-depth (CTD) data to quantify the seasonal difference. The HFR system deployed off southern San Diego covers a roughly $40 \text{ km} \times 40 \text{ km}$ region (black outline in Figure 1). The NDBC buoy is located at 45 km west of the northwest edge of the domain. Since the NDBC wind has approximately 30% missing data and is only weakly coherent with local winds and surface currents, it is only used as a comparison data set for the spatial transfer function and the wind skill map (section 3.2). All data in this paper are from 2 year observations (April 2003 to March 2005). The computations between the wind and surface currents in the following sections have been conducted using each HFR surface current time series at grid points individually,

except for Figure 3, where surface currents on all grid points are averaged together before the power spectrum is estimated. The power spectrum, coherence, and phase are averaged over 56 Fourier coefficients computed from nonoverlapped time series for 13 days. The length of the time series was chosen to separate the inertial frequency and diurnal frequency bins. Since surface currents are correlated in space, the exact ensemble average could not be defined. However, their degrees of freedom are computed according to *Bretherton et al.* [1999] and *Kim et al.* [2010]. The error bar is estimated from either the 95% confidence interval or the Jackknife method [e.g., *Priestley*, 1981; *von Storch and Zwiers*, 1999; *Bendat and Piersol*, 2000]. Both give consistent error estimates. The applied gridding technique on surface currents [e.g., *Kim et al.*, 2008; *Kim*, 2010] (optimal interpolation (OI)) is designed to minimize artificial spatial structure at the kilometer scale by setting an exponential correlation function with 3–10 times shorter length scale than the observed length scale in order to preserve the variance of the field. The use of the exponential function in OI over the segmented correlation function in unweighted least-squares fitting (UWLS) allows us to estimate a spatially continuous and realistic current field, whose noise level is above the assumed error variance. This is supported by the fact that both spatial correlation structures and length scales of surface currents derived from OI and UWLS are consistent [e.g., *Kim et al.*, 2010].

2.1. Wind and Surface Currents

[7] The winds observed at the shore-based stations and the offshore buoy include a large-scale wind and a coastally enhanced land/sea breezes [e.g., *Dorman*, 1982]. After rotary spectral analysis, the variance in the low-frequency band ($|\omega| \leq 0.4$ cycles per day (cpd)) is the largest offshore (NDBC), smaller onshore in an open environment (SIO), and the smallest in an environment (TJR) sheltered by the TJR valley and the Point Loma headland. However, the variance of the diurnal wind increases from NDBC to SIO, then to TJR, reflecting the influence of the land/sea breezes. The existence and size of the land/sea breeze cell is seen in the diurnal variances of winds observed at NDBC buoys along the U.S. West Coast (USWC) which decrease as a linear function of the distance from the coast (not shown).

[8] The dominant surface current variance in the study domain is concentrated as broad peaks in three frequency bands in low frequency and centered at diurnal and semi-diurnal frequencies [e.g., *Kim et al.*, 2007, 2009, 2010]. The principal variance axes of surface currents are roughly parallel to the local coastline, and the spatial covariance function has the shape of an exponential decay.

2.1.1. Spectral Characteristics

[9] The coherence, amplitude, and phase between nearshore winds (SIO–TJR) and offshore–nearshore winds (NDBC–TJR) show a glimpse of the spatial and temporal relationships of coastal winds (Figure 2). The amplitude denotes the variance ratio of the wind relative to the TJR wind. Two nearshore wind observations are coherent (0.6–0.9) at most frequencies, with local maxima at zero and at the diurnal frequency and its harmonics (Figure 2a). In contrast, the NDBC–TJR coherence is relatively weak

(0.2–0.4) in the low-frequency band and at diurnal harmonics and nearly zero in other frequencies (Figure 2b). The two nearshore wind observations have similar variance in most frequency intervals (Figure 2c). On the contrary, the amplitude of the offshore wind in the low-frequency band is 1.2–1.5 times higher than nearshore winds. Above about 0.75 cpd, the amplitude of the offshore wind becomes ~ 0.25 (Figure 2d). Moreover, the phase of NDBC–TJR winds (positive phase means TJR wind leads NDBC wind) (Figure 2f) shows that the NDBC wind leads the TJR wind except at the diurnal frequency and its harmonics. This has been seen elsewhere [e.g., *Weisberg and Pietrafesa*, 1983] and will be discussed in section 4.1.2. There is a small time lag between SIO and TJR winds at the higher negative rotary frequencies, as evidenced by a slope in phase (Figure 2e), but this is not important for the analysis.

[10] The wind in the Southern California Bight (SCB) (south of Point Conception) is typically weak compared to coastal winds north of Point Conception [e.g., *Dorman and Winant*, 1995]. For example, over 80% of the hourly wind records at SIO, TJR, and NDBC are less than 5 m s^{-1} . In the low wind speed regime (less than 5 m s^{-1}), the drag coefficient can increase [e.g., *Large et al.*, 1995; *Yelland and Taylor*, 1996], hold constant [e.g., *Large and Pond*, 1981], or decrease [e.g., *Garratt*, 1977]. Thus the wind stress can be sensitive to the choice of the drag coefficient, which affects the wind regression discussed in this study. Although the larger drag coefficients increased the wind skill by up to 10–15% (see section 3.2 for the wind skill estimate), this does not affect the overall results and conclusion.

2.1.2. Seasonal Spectral Characteristics

[11] The power spectra of the TJR wind and the spatially averaged detided surface currents in summer and winter are shown in Figures 3a and 3c. The surface currents at major tidal constituents (M_2 , K_1 , S_2 , O_1 , N_2 , and P_1 except for S_1) are removed using least-squares fitting [e.g., *Pawlowicz et al.*, 2002; *Kim et al.*, 2010], so that the detided surface currents may contain the variance driven by land/sea breezes (see also section 4.1.1). The rotary spectra in both seasons have a similar variance distribution. However, the overall variance of the wind in winter is 20–30% larger than that in summer, and the width of peaks at the diurnal frequency and its harmonics are slightly narrower in summer than in winter (Figure 3a). The directional probability density function (not shown) of the TJR wind exhibits the dominance of eastward (onshore) wind in summer and of a combination of northward (upcoast) and eastward wind in winter. This partly results from storm events approaching from the south and west during winter, which also modifies variances in the subdiurnal frequency band [e.g., *Dorman*, 1982]. The power spectrum of surface currents shows clockwise dominance, and its seasonal difference is weak (Figure 3b). The magnitude of the coherence between surface currents and the TJR wind varies more between seasons than the phase (Figures 3c and 3d). Note that the strong peaks in variance and coherence appear at the diurnal frequency and not at the local inertial frequency ($f_c = 1.07$ cpd, marked by a vertical line on the plot). Reduced coherence compared to the diurnal peak is presumably a result of poor signal-to-noise ratio

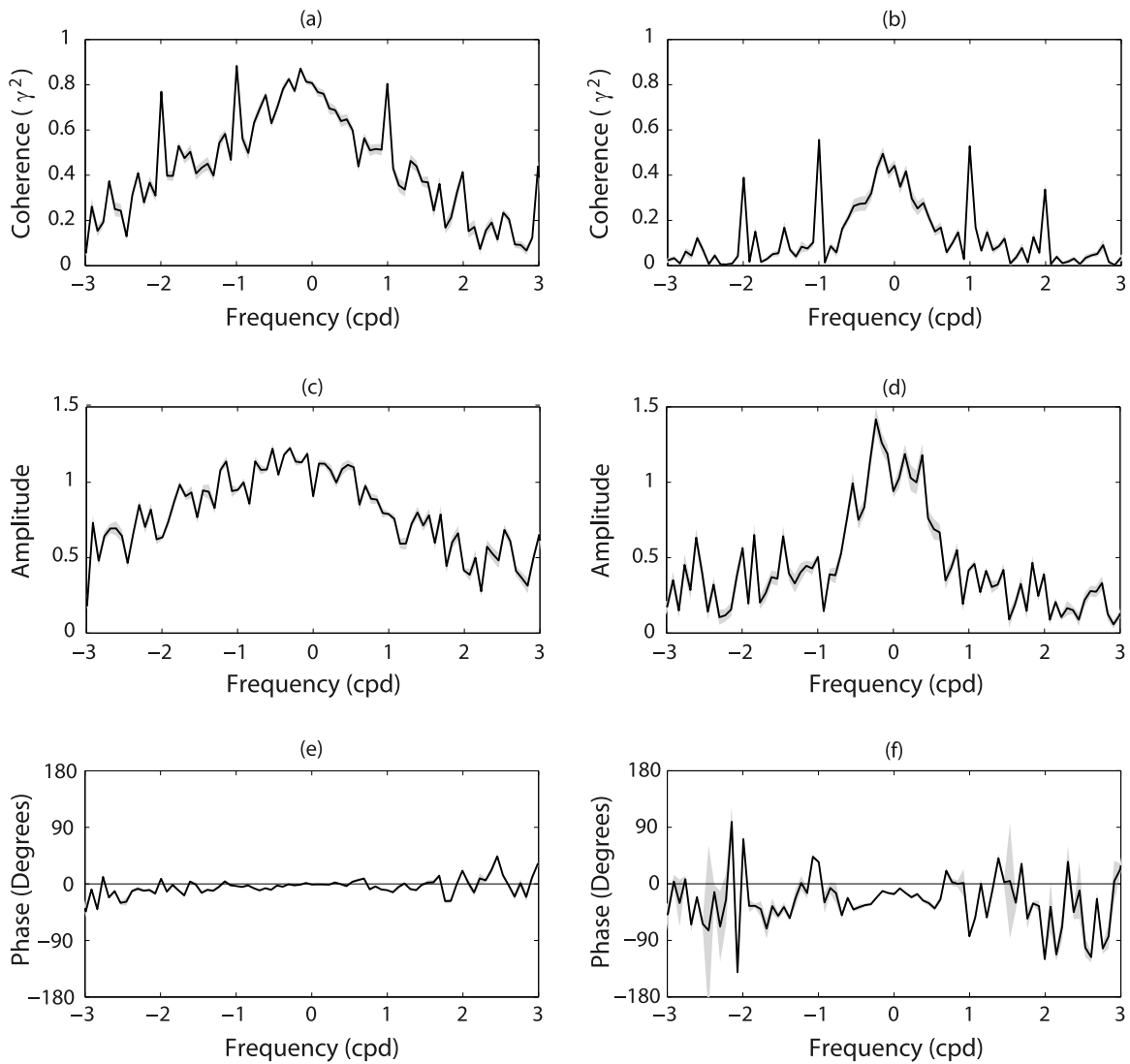


Figure 2. (a) Coherence, (c) amplitude, and (e) phase between SIO and TJR winds. (b) Coherence, (d) amplitude, and (f) phase between NDBC and TJR winds. The amplitude denotes the variance ratio of the wind relative to the TJR wind. The gray error bars are calculated from the Jackknife method. Figures 2a, 2b, 2e, and 2f are adapted from *Kim et al.* [2010].

(SNR) at the inertial frequency due to weak currents and winds.

2.2. Stratification

[12] Monthly CTD profiles have been sampled at 40 local stations as a part of South Bay Ocean Outfall (SBOO) Monitoring Program. Profiles at the C1 station (marked at Figure 1) are used to compute the representative stratification in summer and winter. Temperature, salinity, density, and buoyancy frequency (N^2) profiles for C1 station are shown in Figure 4. The C1 station (~ 100 m depth) was chosen because it shows the least influence of freshwater from the TJR and the SBOO in the archived data set. The upper 20 m is more strongly stratified in summer than in winter. The maximum buoyancy frequency (N) in summer is ~ 20 cycles per hour (cph) at 5–15 m depth. Other SBOO stations are located on the continental shelf (10–65 m depth). The stratification in summer and winter at those

stations is similar to the C1 station in its strength and vertical structure.

3. Methods

[13] The surface currents at the exact tidal lines are removed by a least-squares fit [e.g., *Priestley*, 1981; *Wunsch*, 1996; *Pawlowicz et al.*, 2002]. The detided surface currents (\mathbf{u}_F , section 2.1.2) are decomposed further as

$$\mathbf{u}_F = \mathbf{u}_W + \mathbf{u}_G, \quad (1)$$

where \mathbf{u}_W and \mathbf{u}_G denote the locally wind-driven surface currents and the residual surface currents, respectively.

[14] The wind impulse response and transfer functions have been widely discussed and interpreted with Ekman theory [e.g., *Ekman*, 1905; *Gonella*, 1972; *Weller*, 1981; *Kim et al.*, 2009]. The transfer function describes the relationship

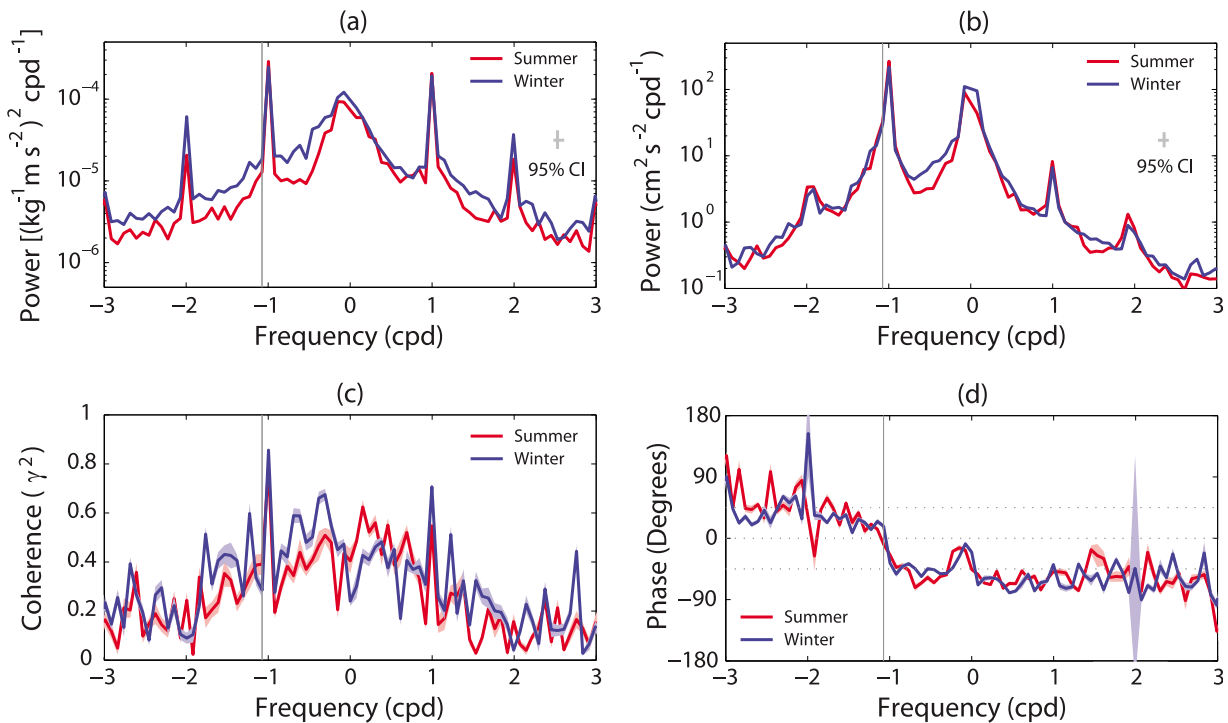


Figure 3. Rotary spectra of the (a) TJR wind and (b) spatially averaged detided surface currents in summer and winter. (c) Coherence and (d) phase between them in summer and winter. The 95% error bars are indicated with shaded areas, and the vertical black line denotes the inertial frequency ($f_c = -1.07$ cpd). Negative and positive frequencies correspond to clockwise and counterclockwise rotations, respectively.

between winds and currents in the frequency domain. The impulse response function is the Fourier transform of the transfer function into the time domain. Although both estimates should be equivalent, in practical cases the two approaches differ in the treatment of missing observations and in the regularization of the inverse problem. Herein the locally wind-driven surface currents are examined with both wind impulse response functions and transfer functions.

[15] The surface current response to wind in coastal regions has been reported as asymmetric and anisotropic in numerical models and observations [e.g., *Allen, 1980; Beardsley et al., 1987; Li and Weisberg, 1999; Weisberg et al., 2001; Kim et al., 2009*]. In other words, the wind-driven current response can differ in terms of the wind direction. For example, the cross-shore currents driven by alongshore wind and cross-shore wind can be different as a result of the local pressure setup and anisotropic boundary conditions (e.g., bottom topography and coastline). Therefore we allow for anisotropy in the estimates of the transfer function and response function. However, the isotropic transfer function is more routine and simpler to present the relationship between wind and currents than the anisotropic transfer function. For instance, the isotropic and anisotropic transfer functions at a given frequency are presented as one complex number and four real numbers, respectively [e.g., *Kim et al., 2009*]. Thus, at first, we focus on the isotropic transfer function for most of the statistical analyses discussed in this paper (sections 4.1 and 4.2), then compute the anisotropic response function (section 4.3). Frequency domain transfer function and time domain response function

are verified to be consistent for locally wind-driven surface currents in this region. As the statistical descriptions of the response function were addressed thoroughly by *Kim et al. [2009]*, the essential parts of the transfer function estimation are only reviewed briefly here.

3.1. Wind Transfer Functions

[16] The frequency domain transfer function (\mathbf{H}) is computed from the averaged covariance of the Fourier coefficients of detided surface currents ($\hat{\mathbf{u}}_F$) and wind stress ($\hat{\boldsymbol{\tau}}$) at multiple wind stations frequency-by-frequency (ω). For the isotropic estimate these variables are combined into complex numbers ($\hat{\boldsymbol{\tau}} = \hat{\tau}_x + i\hat{\tau}_y$, $\hat{\mathbf{u}} = \hat{u} + i\hat{v}$), respectively. On the other hand, those vector components can be considered separately in the x and y directions for the calculation of the anisotropic transfer function. Either transfer function is estimated by

$$\mathbf{H}(\mathbf{x}, \omega) = (\langle \hat{\mathbf{u}}_F(\mathbf{x}, \omega) \hat{\boldsymbol{\tau}}^\dagger(\omega) \rangle) (\langle \hat{\boldsymbol{\tau}}(\omega) \hat{\boldsymbol{\tau}}^\dagger(\omega) \rangle + \mathbf{R}_c)^{-1}, \quad (2)$$

where \mathbf{R}_c denotes a regularization matrix, \dagger is the complex conjugate transpose, and $\langle \cdot \rangle$ indicates the ensemble average. So the isotropic estimate is calculated by inverting a M by M complex matrix, while the anisotropic estimate inverts a $2M$ by $2M$ matrix (for M wind stations). The argument (Θ) of the isotropic transfer function is the angle measured counterclockwise from the positive real number axis. It is the sum of the phase difference in the frequency domain (or time lag in the time domain) and the veering angle between the wind and currents. However, the argument at zero fre-

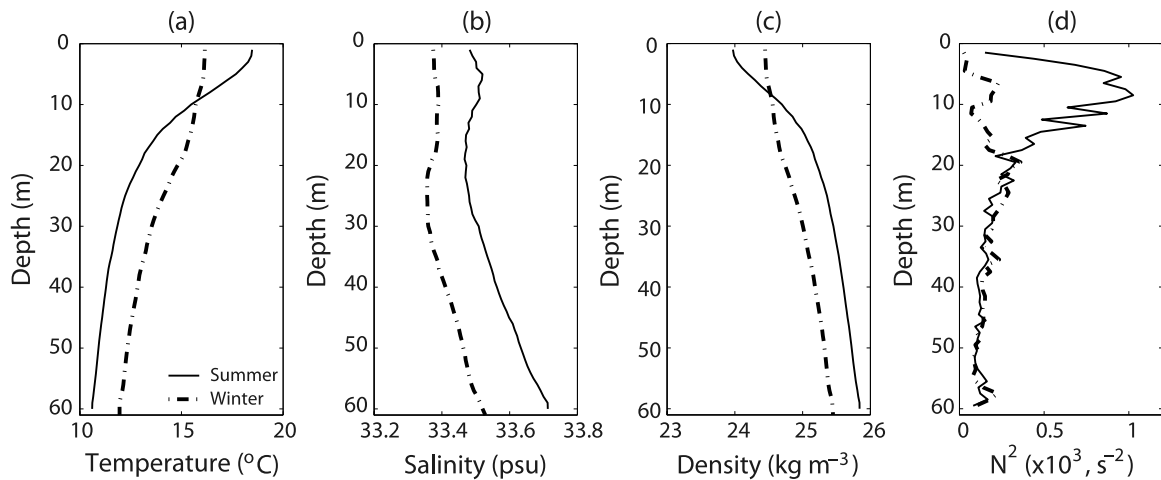


Figure 4. Vertical profiles of (a) temperature ($^{\circ}\text{C}$), (b) salinity (psu), (c) density (kg m^{-3}), and (d) buoyancy frequency (N^2)($\times 10^3, \text{s}^{-2}$) at the C1 station (Figure 1) in summer and winter. The labels “summer” and “winter” are referred to as April–September and October–March, respectively.

quency is only the veering angle (because there is no time lag). Thus, the argument of the transfer function requires careful interpretation.

[17] The Fourier coefficients of the locally wind-driven surface currents are given by the product of the transfer function and wind stress

$$\hat{\mathbf{u}}_W(\mathbf{x}, \omega) = \mathbf{H}(\mathbf{x}, \omega) \hat{\boldsymbol{\tau}}(\omega). \quad (3)$$

In addition, the regression using three winds ($M = 3$) is formulated as

$$\begin{aligned} \hat{\mathbf{u}}_W(\mathbf{x}, \omega) &= \sum_{m=1}^M \mathbf{H}_m(\mathbf{x}, \omega) \hat{\boldsymbol{\tau}}_m(\omega) \\ &= [\mathbf{H}_1(\mathbf{x}, \omega) \quad \mathbf{H}_2(\mathbf{x}, \omega) \quad \mathbf{H}_3(\mathbf{x}, \omega)] \begin{bmatrix} \hat{\boldsymbol{\tau}}_1(\omega) \\ \hat{\boldsymbol{\tau}}_2(\omega) \\ \hat{\boldsymbol{\tau}}_3(\omega) \end{bmatrix}. \end{aligned} \quad (4)$$

[18] The regression is a least-squares calculation with prior (expected) variances for the observation error and the unknown transfer function (\mathbf{H}) (see Appendix B). The prior transfer function variance for each wind time series reflects the expected size of the transfer function (\mathbf{H}) for that wind time series. When wind time series are coherent at a frequency, there is ambiguity in attributing the transfer function at that frequency. In the limiting case of perfect coherence between two time series, there is complete ambiguity. When ambiguity is present, the prior will make a difference in the relative sizes (allocation) of the transfer function for the different winds, but the overall skill will not be changed. Successive orthogonalization [e.g., *Lanczos*, 1956] of the driving time series can eliminate the ambiguity at the expense of an arbitrary allocation of transfer function based on the order of the orthogonalization. Because we limit our discussion of multiple winds to skill, the prior is not important, and we assume equal prior var-

iances for each transfer function (see section 4.2 and Appendix B).

3.2. Wind Skill Metric

[19] The fractional variance of surface currents explained by regression with one or more wind measurements is used as a skill metric (κ^2). This can be calculated for each frequency (ω_l), or as the ratio of variances summed over a frequency band. This skill is the complement of the residual variance ratio of locally wind-driven surface currents (section 4.2)

$$\kappa^2(\mathbf{x}) = 1 - \frac{\sum_l |\hat{\mathbf{u}}_G(\mathbf{x}, \omega_l)|^2}{\sum_l |\hat{\mathbf{u}}_F(\mathbf{x}, \omega_l)|^2}, \quad (5)$$

where $\hat{\mathbf{u}}_G(\mathbf{x}, \omega) = \hat{\mathbf{u}}_F(\mathbf{x}, \omega) - \hat{\mathbf{u}}_W(\mathbf{x}, \omega)$, and l is the index in the finite frequency domain.

3.3. Regularization

[20] The regularization matrix combats the errors and noise contaminating the wind stress and tunes the variance of the regression estimate (in this case, locally wind-driven surface currents) [e.g., *Inman*, 1975; *Tikhonov and Arsenin*, 1977; *Constable et al.*, 1987; *Wunsch*, 1996]. \mathbf{R}_c appears in equation (2) as the noise level of the wind stress, although it is also compensating for the errors in the sample covariance matrices used in the regression. For simplicity, it is assumed herein to be a diagonal matrix with constant variance

$$\mathbf{R}_c = \alpha^2 \mathbf{I}. \quad (6)$$

The amount of regularization (α^2) is adjusted to minimize the cross-validation error [e.g., *Efron and Gong*, 1983; *LeBlanc and Tibshirani*, 1996; *Kim et al.*, 2009], and is implemented as a fraction of the variance of wind stress in each frequency band.

[21] If the wind data at M stations are used as the basis of regression, \mathbf{R}_c is a M by M square matrix for the isotropic

estimate (or $2M$ by $2M$ matrix for the anisotropic estimate) with diagonal regularization terms scaled by the variance of each data source at that frequency. For example, the isotropic regularization in the regression using winds at three stations becomes

$$\mathbf{R}_c = \begin{bmatrix} \alpha_1^2 & 0 & 0 \\ 0 & \alpha_2^2 & 0 \\ 0 & 0 & \alpha_3^2 \end{bmatrix}, \quad (7)$$

where α_1^2 , α_2^2 , and α_3^2 are the adjusted noise levels of each wind data.

4. Results

[22] As mentioned above (section 3), most results presented herein are based on the frequency domain transfer functions except the time domain calculation of the mean wind-driven surface currents (section 4.3). The differences between the Fourier transformed transfer function and the directly estimated response function are negligible within the error bar range [e.g., *Kim et al.*, 2009] although they are different in the treatment of missing data. For the frequency domain analysis the missing observations are substituted with the mean value computed from only observations. In the time domain analysis, missing observations are not used for the covariance estimate. While the transfer function can include the low-frequency signals of both winds and surface currents in some extent, the wind-driven surface currents off San Diego would be considered as “local” components. That is the reason for the term “locally wind-driven surface currents” used in this paper.

4.1. Wind Transfer Functions

4.1.1. Probability Density Functions of Transfer Functions

[23] Isotropic transfer functions are estimated from a single wind observation (SIO, TJR, or NDBC) and detided surface currents at each grid point within the radar coverage area shown in Figure 1. Both magnitude and argument of estimated transfer functions are presented as probability density functions at each frequency bin in Figures 5a and 5b (SIO), 5c and 5d (TJR), and 5e and 5f (NDBC).

[24] Although the magnitude of the NDBC transfer function is about 20–90% less than that of the SIO and TJR transfer functions, the spectral shape of all three transfer functions is similar. The peak and argument shift near the inertial frequency are consistent with previous studies [e.g., *Gonella*, 1972; *Weller*, 1981; *Rio and Hernandez*, 2003; *Elipot*, 2006; *Kim et al.*, 2009].

[25] The removal of the S_2 surface tide component from the observed surface currents (see section 2.1.2) causes the drop of the transfer function at that frequency (Figures 5a, 5c, and 5e). The relatively small magnitude of the NDBC transfer function makes the drop look difficult to see in Figure 5e. The peaks near 1 and 2 cpd result from the high coherence between the wind and surface currents at seasonal harmonics of $1 \pm \Delta\omega$ and $2 \pm \Delta\omega$ ($\Delta\omega = 1/365.2425$ days = 0.0027 cpd). Moreover, the peak at low frequency ($|\omega| \leq 0.4$ cpd) is not found in the theoretical transfer function. It is

at least partly due to the presence of the coast, which can support wind-driven pressure gradients [e.g., *Ryan and Noble*, 2006], both local and remote, which in turn balance the Coriolis force on currents as originally described by Ekman in the low-frequency limit [e.g., *Ekman*, 1905; *Winant*, 2004]. Because the coherence (not shown) between the sea surface elevations off San Diego and the local wind (SIO and TJR) is ~ 0.1 in this low-frequency band, a local (small scale) pressure setup is more likely. The local pressure setup in the alongshore and cross-shore directions can cause anisotropic current response to the wind, reflecting the coastline boundary effect [e.g., *Kim et al.*, 2009].

[26] The data-derived arguments are roughly consistent with the theoretical model results (gray lines in Figures 5b, 5d, and 5f), except for abrupt changes in the low-frequency band ($|\omega| \leq 0.4$ cpd) and fluctuations in the high-frequency band ($|\omega| > 2$ cpd). The argument of the NDBC transfer function is the most consistent in the low-frequency band and near the inertial frequency, where the signals (and coherence to local winds) are the highest.

[27] As an alternative analytic wind-ocean model besides the Ekman model, the slab layer model [e.g., *Pollard and Millard*, 1970; *D’Asaro*, 1985] was implemented with a single layer current response in the upper ocean to the wind and a friction term to compensate the time decay of inertial motions, which is identical to the depth-averaged Ekman model. However, although the slab layer model has similarity to the Ekman model, the argument in the slab layer model is constant as 90° ($\omega < -f_c$) and -90° ($\omega > -f_c$) within the mixed layer [e.g., *Gonella*, 1971] in contrast to the estimated arguments from the regional and global observations (Figures 5b, 5d, and 5f) [e.g., *Weller*, 1981; *Davis et al.*, 1981; *Rio and Hernandez*, 2003; *Kim et al.*, 2009].

4.1.2. Spatial Structure of Transfer Functions

[28] The spatial structure of the isotropic transfer function at three representative frequencies is examined by magnitude (Figure 6) and argument (Figure 7). The three frequencies are inertial frequency ($\omega = -f_c$), clockwise diurnal frequency ($\omega = -1$ cpd), and low frequency. The transfer function at $\omega = 0$ cpd is used as a representative of transfer functions in the low-frequency band for most of the discussion below. The wind energy is the highest in the diurnal band, so the transfer function at that frequency is the most reliable. The argument maps highlight fluctuations which appear to reflect details of the radar coverage, including features echoing the measured beam patterns and baselines (black arrows marked in Figure 7). This can be used as a diagnostics of the beam patterns of a HFR observing system.

[29] The magnitude of the transfer function at inertial and diurnal frequencies is reduced nearshore relative to offshore because of the influence of the coastline and bathymetry (Figures 6a, 6b, 6d, 6e, 6g, and 6h) [e.g., *Davies*, 2003]. The low-frequency transfer function is enhanced near the coast (Figures 6c, 6f, and 6i), for similar reasons, consistent with the set up of local pressure gradients.

[30] As described in section 3.1, the argument of the transfer function (except at the zero frequency) sums both time lag and veering angle. If the veering angle at and above the diurnal frequency is constant, the argument in that frequency band can be interpreted as the time lag. Thus the argument difference between nearshore winds (SIO and TJR, less than 45°) and offshore wind (NDBC, more than

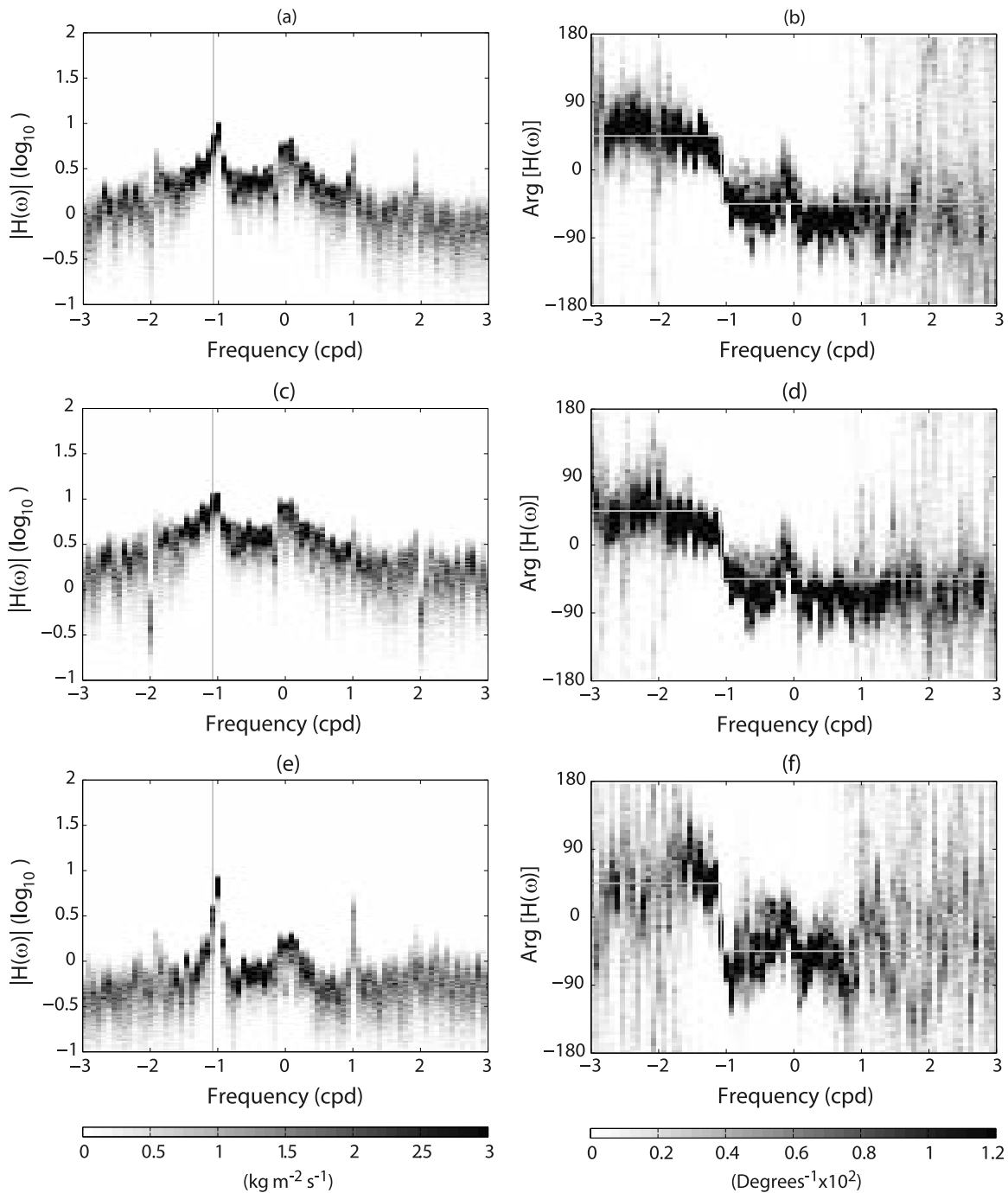


Figure 5. (a, c, and e) Magnitude ($\text{kg}^{-1} \text{m}^2 \text{s}$) and (b, d, and f) argument (degrees) of isotropic transfer functions estimated from individual wind at SIO (Figures 5a and 5b), TJR (Figures 5c and 5d), and NDBC (Figures 5e and 5f) and surface currents are presented as probability density functions at each frequency bin. The gray lines denote the inertial frequency ($f_c = -1.07$ cpd) and the theoretical argument of the wind-driven surface currents, respectively [e.g., *Gonella, 1972; Kim et al., 2009*]. Shared color bars are shown on the bottom.

45°) with a nearly constant value over the domain shows different time lags (Figures 7b, 7e, and 7h). The diurnal land/sea breezes, driven by the significant difference in the thermal heat capacity [e.g., *Estoque, 1961; Atkinson, 1981*], can have time lags between nearshore and offshore depending on the size and development of the land/sea breeze cell. Moreover, the TJR diurnal wind leads the NDBC

diurnal wind by about 2 h ($\Delta\Theta \approx 30^\circ$ in Figure 2f) [e.g., *Weisberg and Pietrafesa, 1983*]. As a result, the surface currents regressed with the diurnal wind at NDBC have a persistent difference in the argument compared to the surface current response to the diurnal wind at TJR or SIO. The arguments at the diurnal frequency are consistent with

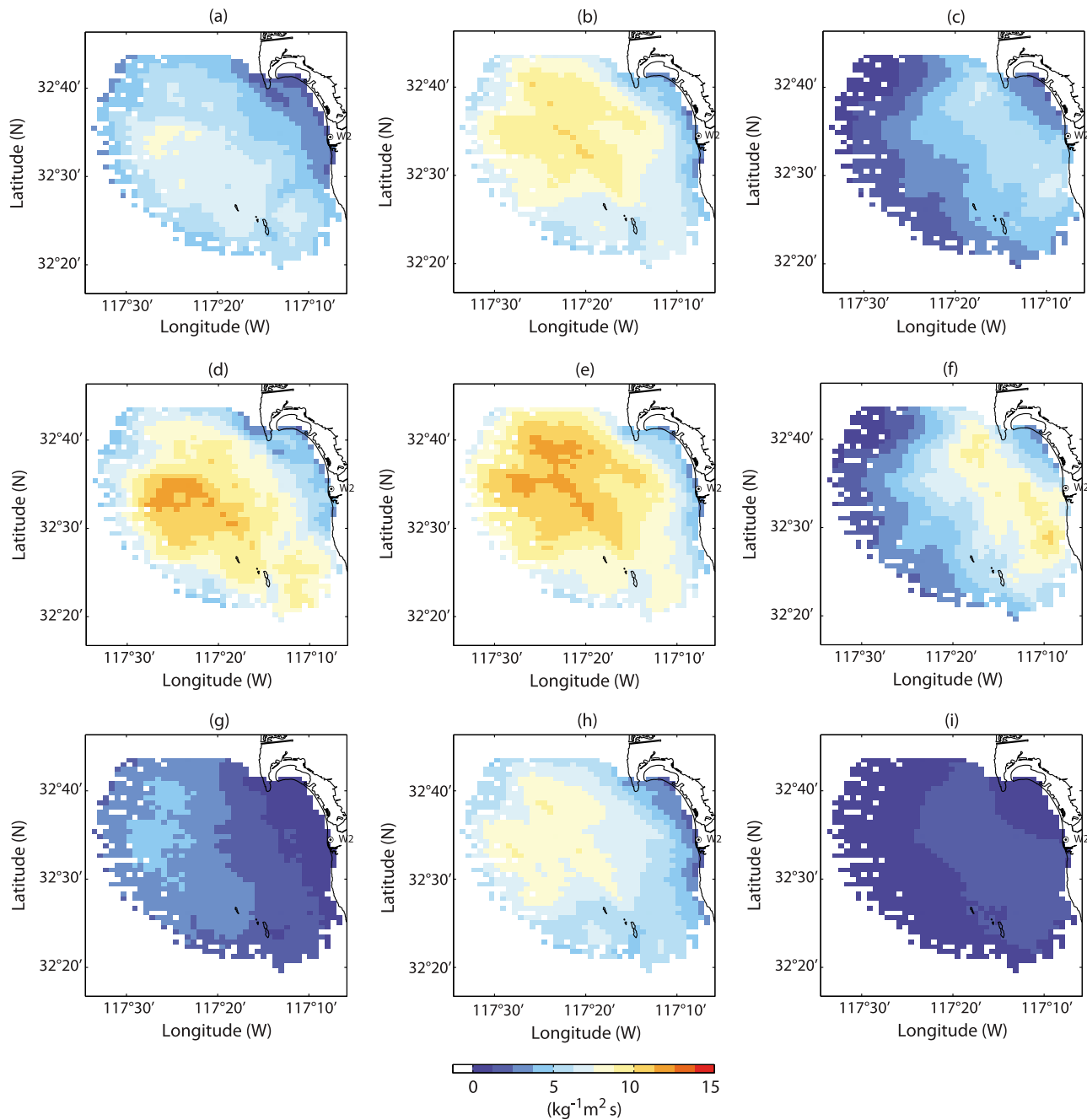


Figure 6. Magnitude ($\text{kg}^{-1} \text{m}^2 \text{s}$) of the transfer function at (left) $\omega = -f_c$, (middle) $\omega = -1$ cpd, and (right) $\omega = 0$ cpd for individual wind at (a–c) SIO, (d–f) TJR, and (g–i) NDBC.

results from subsurface currents (5 m depth) and winds of *Pidgeon and Winant* [2005].

[31] Ignoring the small-scale structures in the argument map (e.g., artifacts due to the measured beam pattern and baselines in Figure 7), the arguments at low frequency exhibit a spatial gradient from less than 45° nearshore to more than 45° offshore in the sense of rotation to the right of the direction of both SIO and TJR winds (Figures 7c and 7f). This reduced rotation nearshore can be explained by the sampling depth relative to the full Ekman layer depth nearshore and offshore. The surface currents averaged over upper $O(1)$ m depth correspond to a shallower depth relative to the full Ekman layer in nearshore than offshore. In other words,

the reduced stratification nearshore increases the Ekman depth and the Ekman spiral rotates slower in the vertical due to deeper momentum transfer [e.g., *Lentz*, 2001; *Kirincich et al.*, 2005]. These cross-shore dynamics can generate an anisotropic current response to the wind in coastal regions. As a part of the anisotropic response, the spatial gradient of the argument may be related to the spatial balance between local pressure setups parallel and normal to the wind [e.g., *Ryan and Noble*, 2006; *Kim et al.*, 2009].

[32] The influence of the bottom boundary layer on the surface currents was examined with hourly subsurface currents (ADCP) and temperature profiles at 28 m depth for about one and a half years (2007–2008) using criteria from

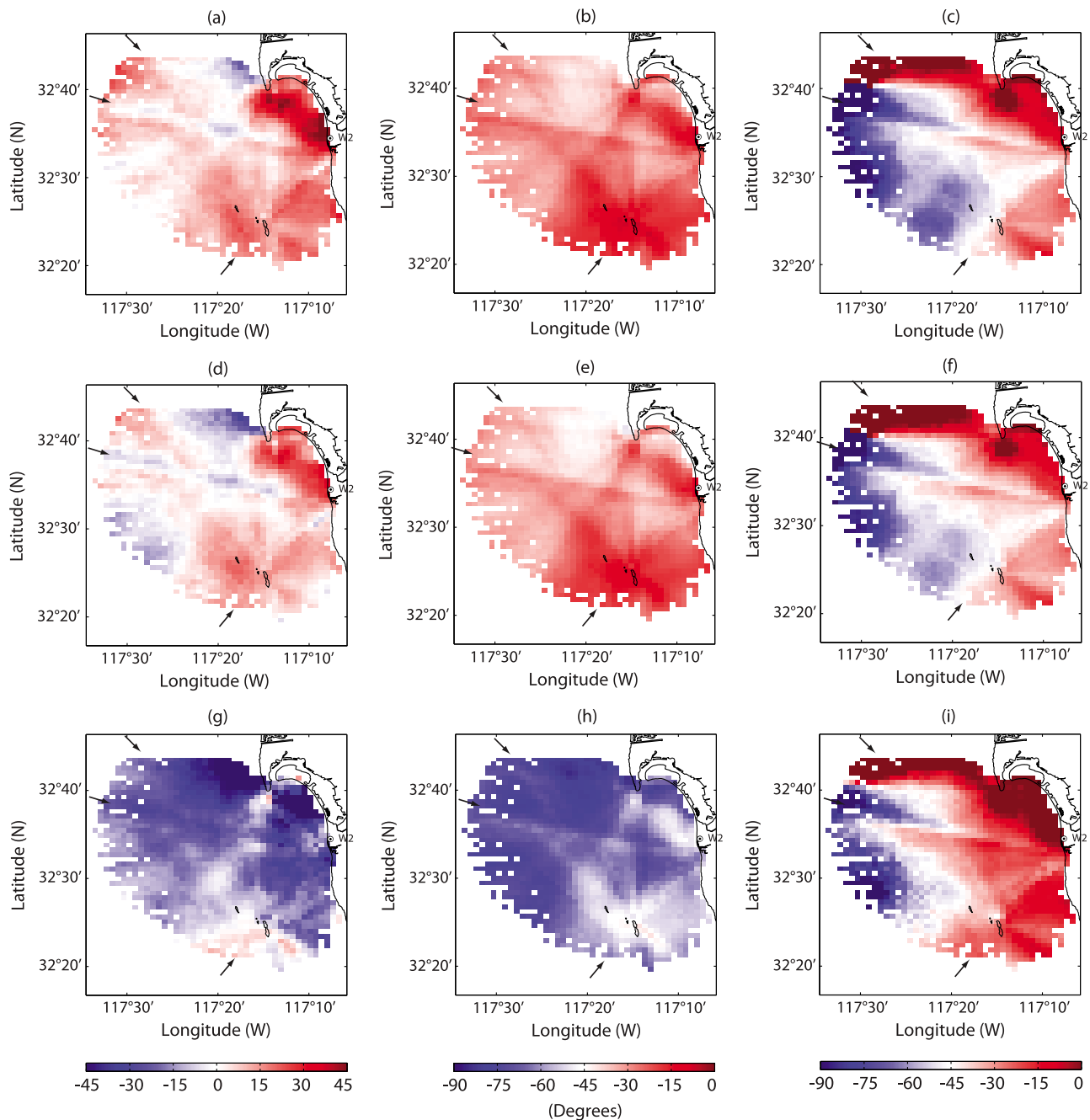


Figure 7. Argument (degrees) of the transfer function at (left) $\omega = -f_c$, (middle) $\omega = -1$ cpd, and (right) $\omega = 0$ cpd for individual wind at (a–c) SIO, (d–f) TJR, and (g–i) NDBC. Three black arrows indicate the artifacts as a result of the measured beam patterns and baselines. Shared color bars are shown on the bottom.

Perlin et al. [2005, 2007] (not shown). Although the bottom mixed layer varies with seasonal stratification, it rarely reaches up to 5 m below the surface. Moreover, the dissipation rate is not strong enough to build a deep turbulent bottom layer. Thus, the surface currents in this region are probably only weakly affected by bottom boundary layer except for the near-coast region with less than 5 m depth, i.e., about 3% of the study domain.

[33] The transfer functions are smaller nearshore at inertial and diurnal frequencies and larger nearshore in the sub-

inertial frequency band, consistent with the results from a two-dimensional analytical model [Ponte, 2010]. This model is defined in the frequency domain and run with a unidirectional alongshore wind stress over the domain having a linear sloping bottom and straight coast.

4.1.3. Regularization

[34] For the regularization, α_1^2 , α_2^2 , and α_3^2 in equation (8) are 0.1, 0.125, and 0.15, which are chosen to minimize the cross-validated prediction error. In the cross validation, the transfer function computed from the training data (90% of

total data) is applied to the test data (the data excluding training data), and its residual variance becomes the cross-validated error (equation (6)). Since a transfer function can be determined ambiguously when partially correlated winds at multiple stations are used in the regression, we use another measure, the skill of the wind in explaining the wind-driven currents.

4.2. Wind Skill Maps

[35] The wind skill map, i.e., the fractional variance of surface currents explained by wind (section 3.2), is also considered in several frequency bands and with respect to individual wind stations (SIO, TJR, or NDBC) and all wind stations together (SIO, TJR, and NDBC). As the number of predictor time series in the regression increases, statistical noise and observational errors in the covariance matrices can reduce cross-validated skill in the estimate. However, an appropriate regularization reduces these impacts [e.g., Davis, 1985; Kim *et al.*, 2009]. In case that the observations with missing data are used as the regression basis, the quality of concurrent data sets is crucial to minimize the uncertainty of the regression. Since the SIO and TJR wind data have nonconsecutive (intermittent) missing data with less than 8% for 2 years, the overall estimates are weakly affected by missing data. The wind skill using all wind data (SIO, TJR, and NDBC) is only estimated from concurrent data. Although the error covariance matrix can be modified with the quality of the model data, this is beyond the scope of this paper.

[36] Frequencies at and below 2 cpd ($|\omega| \leq 2$ cpd) include most of the variance of wind-driven components. The SIO and TJR skill maps for that range (Figure 8) show the skill decreasing with distance from the TJR wind station, ranging from (~ 0.5) nearby to (~ 0.25) offshore (Figures 8a and 8b). This spatial structure could be explained by reduced skill of the shore station wind in estimating offshore wind, by a reduced response of offshore surface currents to the wind, or both. The TJR skill map has slightly higher values than the SIO skill map, but the differences are roughly within error bars. While the spatial pattern of the NDBC skill map contains a footprint of the SIO and TJR skill maps, the explained variance is less than 20% (Figure 8c). Moreover, the coherence between TJR and NDBC winds is at most 0.5 at the diurnal frequency and less than 0.2 for other frequencies. Thus, while both hypothesis are attributed to the structure of skill maps, the spatial variation of surface current response may be more relevant in this region than the decorrelation of the wind between shore and offshore. In spite of the distance between the two shore stations (SIO and TJR), the structure of their wind skill maps suggests that both shore stations are measuring similar large-scale winds and land/sea breezes (Figures 8a and 8b).

[37] The skill map for estimates using all three observed winds together shows that approximately 40% of the surface current variance can be explained by wind (Figure 8d). Since only concurrent wind data for all three stations are used, missing value can strongly affect this estimate. In this analysis the prior of each wind is considered to be equal (Appendix B). On the other hand, it could be assumed as a function of distance between the center of the study domain

and the wind stations, which is one of many arbitrary choices for attribution.

[38] Although some cross-shore structure of the wind field can be inferred from three point observations (SIO, TJR, and NDBC), it was also examined with two high-resolution COAMPS model runs (1.7 km and 5.1 km resolutions) off southern San Diego [e.g., Hodur, 1997]. The (Gaussian) decorrelation length scales of the 1.7 km resolution wind product are 15 to 25 km at the coast and 40 to 60 km at 50 km offshore (not shown). The wind at 5.1 km resolution has approximately twice the length scales of the wind at 1.7 km resolution. These decorrelation length scales are larger than the structure seen in the response function, supporting the interpretation that it is due to ocean dynamics, not wind decorrelation, if the model length scales are accurate. As a check on the model, the correlations between the model winds at the three observation locations are 0.58–0.86, somewhat higher than the correlation between the observed winds at those locations, which are 0.48–0.78. Since correlations between model and observed winds are in a range of 0.4–0.7, the model winds may be missing some of the variability in the real wind field, and thus give higher correlations, but only by a small factor.

4.3. Wind Impulse Response Functions

[39] As a parallel approach to transfer functions in the frequency domain, we briefly examine response functions in the time domain. The (anisotropic) response function is computed from detided surface currents at each grid point and both wind stations together (SIO and TJR). Since the temporal amplitude of the transfer function has a near inertial oscillation which decays within 4–5 days [e.g., Kim *et al.*, 2009], we consider the effective wind forcing on surface currents at a given time as the wind record for 6 days prior to that time. The regularization level is set as 10% of the variance of the wind stress, which is $1.41 \times 10^{-5} \text{ kg}^2 \text{ m}^{-2} \text{ s}^{-4}$.

[40] The locally wind-driven surface currents (\mathbf{u}_w) are calculated from the estimated impulse response function and two wind time series (SIO and TJR). The regionally averaged power spectrum of the locally wind-driven surface currents characterizes the response to the diurnal wind (land/sea breezes) and its harmonics superposed on the red power spectrum [Kim *et al.*, 2010, Figure 2b], which has very similar spectral content to the wind spectra. The directly estimated impulse response function and the Fourier transformed transfer function are consistent in this study and elsewhere [e.g., Kim *et al.*, 2009]. We present the time domain approach as well here because it is practical and complementary to the frequency domain analysis.

[41] As an example of results from the time domain, we consider the time mean wind-driven currents over 2 years. In the time domain, the mean wind-driven surface currents vary slowly over the study domain from 7–10 cm s^{-1} south of Point Loma to 1–5 cm s^{-1} offshore and nearshore (Figure 9). Notably, the response is weaker along the continental shelf break. This spatial gradient is ascribed to the spatial structure of the transfer function in the low-frequency band (Figures 6c, 6f, and 6i). This result is similar to the product of the spectrally estimated transfer function and wind Fourier coefficients at zero frequency (equation (3), not shown).

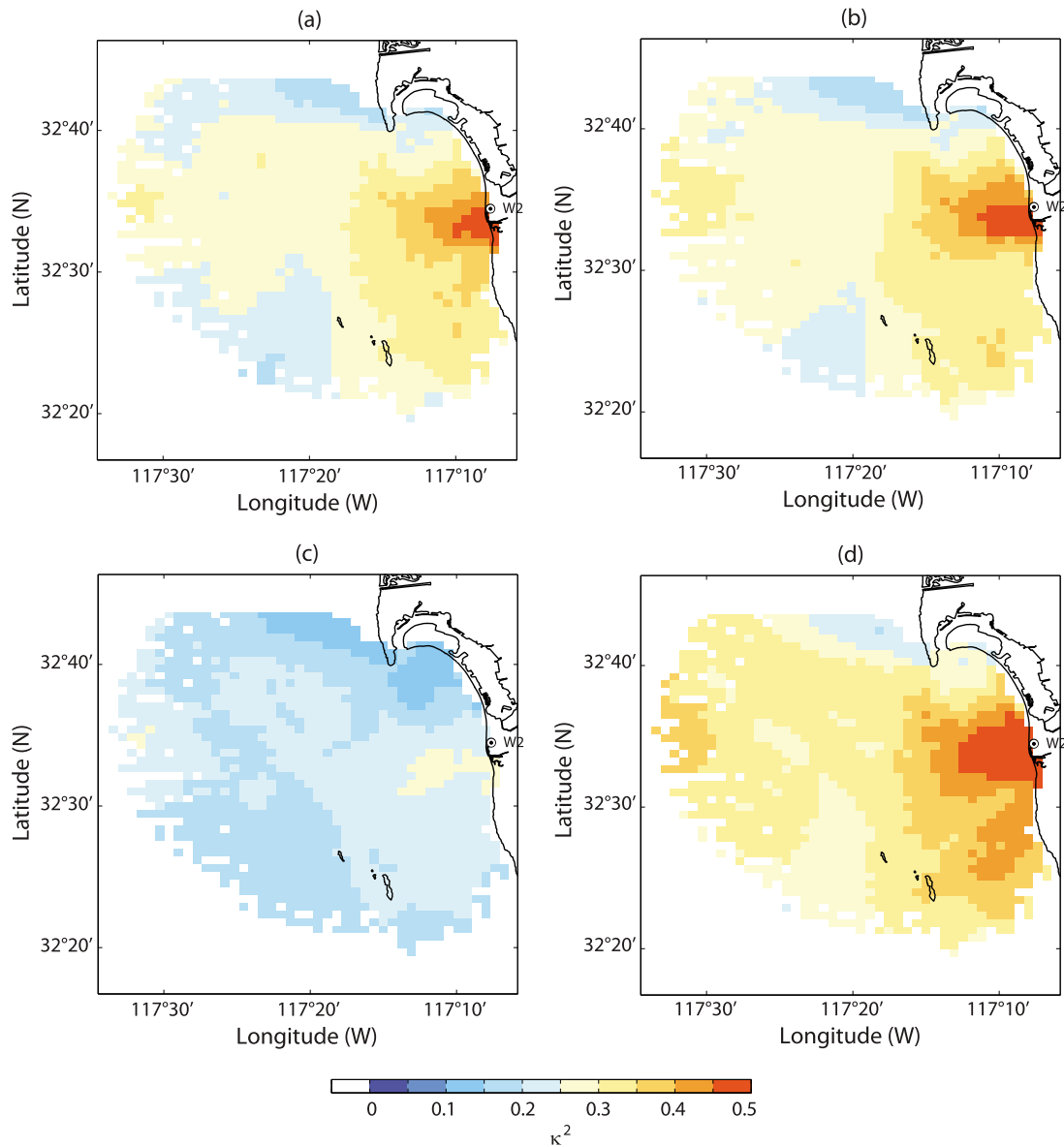


Figure 8. Wind skill map (κ^2) for frequencies at and below 2 cpd ($|\omega| \leq 2$ cpd), which includes most of the energy related to the wind and surface current interactions, with respect to individual wind at (a) SIO, (b) TJR, and (c) NDBC and (d) all wind stations together (SIO, TJR, and NDBC).

[42] The joint probability density function of the ratio of the wind-driven surface current speed ($|\mathbf{u}_W|$) to the wind speed (SIO and TJR; $|\mathbf{u}^W|$) as a function of the wind speed is calculated (not shown). For low wind speed (less than 1 m s^{-1}) the ratio is poorly determined. The ratio varies in the range 2–5% for intermediate wind speed (between 1 and 5 m s^{-1}). At high wind speed (more than 5 m s^{-1}) only ~1% of total wind data) the ratio converges to about 4%. The dominant ratio over all speeds stays within 2–5%. This ratio agrees with the continuity of momentum flux in the air-sea interface [e.g., Kudryavtsev *et al.*, 2008]

$$|\mathbf{u}_W| = \left(\frac{\rho_{\text{air}}}{\rho_{\text{sea}}}\right)^{\frac{1}{2}} |\mathbf{u}^W| = 0.0353 |\mathbf{u}^W|, \quad (8)$$

and is consistent with other studies [e.g., Bye, 1965; Churchill and Csanady, 1983; Wu, 1983; Weber, 1983; Spaulding, 1999].

[43] Over all grid points, the dominant direction of the mean wind-driven currents is $149^\circ \pm 14^\circ$ clockwise from true north. The directions of the mean winds are 61° (SIO) and 71° (TJR) in the same sense (Figure 9). These veering angles are the outer limit of the range of the isotropic and anisotropic surface current responses near the coast, i.e., 42° (isotropic) and 10° – 70° (anisotropic) to the right of the wind direction [e.g., Kim *et al.*, 2009].

4.4. Seasonal Transfer Functions

4.4.1. Uncertainty of Seasonal Transfer Functions

[44] Since both wind and surface currents have seasonality, it needs to be evaluated whether seasonality of the wind

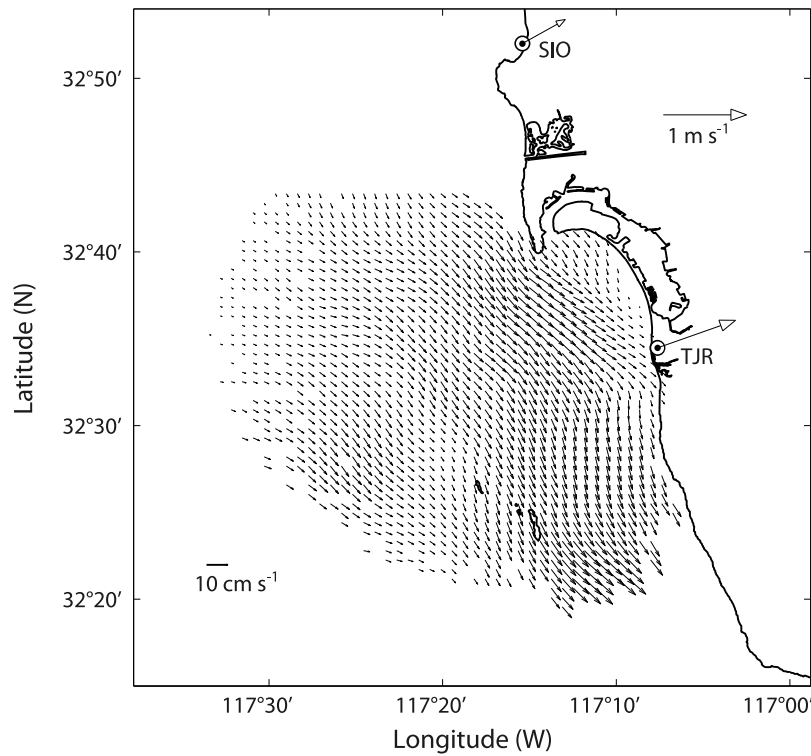


Figure 9. The time mean of locally wind-driven surface currents and TJR and SIO winds. Their references indicate 10 cm s^{-1} and 1 m s^{-1} , respectively.

influences the seasonal transfer function estimates. Thus, the significance of the seasonal transfer function is computed by considering the null hypothesis that seasonal surface currents (\mathbf{u}_s and \mathbf{u}_w) come from a single response function (\mathbf{G}_0) and seasonal winds (τ_s and τ_w)

$$\mathbf{u}_s = \mathbf{G}_0 \tau_s, \quad (9)$$

$$\mathbf{u}_w = \mathbf{G}_0 \tau_w. \quad (10)$$

A transfer function (\mathbf{H}_0) and its inversely Fourier transformed response function (\mathbf{G}_0) are chosen from theory [Kim *et al.*, 2009, Figure B1a], and seasonal winds are from TJR wind data.

[45] Seasonal transfer functions are calculated from the Fourier transformed seasonal surface currents ($\hat{\mathbf{u}}_s$ and $\hat{\mathbf{u}}_w$) and winds ($\hat{\tau}_s$ and $\hat{\tau}_w$) with an appropriate regularization (\mathbf{R}_s and \mathbf{R}_w , respectively)

$$\mathbf{H}_s = \frac{\langle \hat{\mathbf{u}}_s \hat{\tau}_s^\dagger \rangle}{\langle \hat{\tau}_s \hat{\tau}_s^\dagger \rangle + \mathbf{R}_s}, \quad (11)$$

$$\mathbf{H}_w = \frac{\langle \hat{\mathbf{u}}_w \hat{\tau}_w^\dagger \rangle}{\langle \hat{\tau}_w \hat{\tau}_w^\dagger \rangle + \mathbf{R}_w}, \quad (12)$$

where \mathbf{H}_s and \mathbf{H}_w are the estimated transfer functions for summer and winter, respectively, and their arguments are Θ_s and Θ_w .

[46] The uncertainty of seasonal transfer functions due to the wind excitation is computed by the difference in the magnitude and argument

$$\sigma_H = |\mathbf{H}_s - \mathbf{H}_w|, \quad (13)$$

$$\sigma_\Theta = |\Theta_s - \Theta_w|. \quad (14)$$

The magnitude of \mathbf{H}_s and \mathbf{H}_w is expected to be less than that of \mathbf{H}_0 because of regularization. In general, the uncertainties for the magnitude and argument are $O(1)$ and 3° – 5° , respectively. However, the arguments at the inertial frequency ($\Theta_s(-f_c)$ and $\Theta_w(-f_c)$) are off approximately -10° , which might be a variance leakage into the nearby frequency bin. On the other hand, the slopes of the argument at $\omega = -f_c$ are nearly the same as the model. Therefore the difference in the seasonal transfer functions is assumed to be mainly due to the seasonal ocean state, stratification and heat flux, at and near the surface rather than seasonal wind. However, the argument of seasonal transfer functions at $\omega = -f_c$ should be interpreted with care, because of the low SNR.

4.4.2. Probability Density Functions of Transfer Functions

[47] The transfer functions for summer and winter are estimated in the same manner as for the 2 year data from the TJR wind station only and surface currents at all grid points in the domain, and they are presented as probability density functions at each frequency bin (Figure 10).

[48] In general, both summer and winter transfer functions have similar shapes compared to the 2 year transfer function (Figures 5c and 5d). The argument of the summer

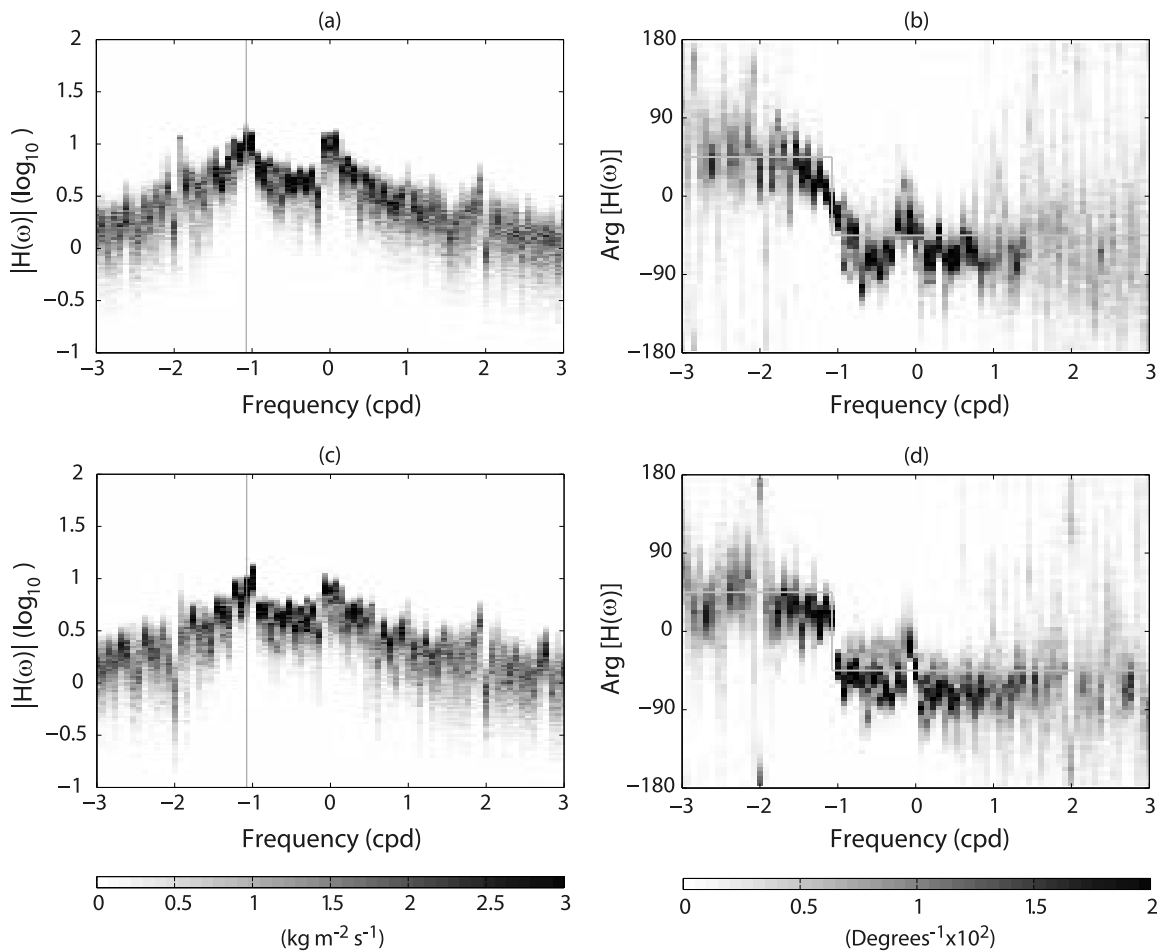


Figure 10. (a and c) Magnitude ($\text{kg}^{-1} \text{m}^2 \text{s}$) and (b and d) argument (degrees) of the isotropic TJR wind transfer functions for (a) summer and (b) winter are presented as probability density functions at each frequency bin. Shared color bars are shown on the bottom.

transfer function slowly shifts near the inertial frequency as opposed to abruptly changing in winter. Moreover, although the scattered data in the positive high-frequency band ($\omega > 2$ cpd) can be ambiguous, the argument for $\omega < -1$ cpd converges to greater than 45° in summer and near 45° in winter (Figures 10b, 10d, and 3d). The argument slope at the inertial frequency is closely related to the friction term added in the classic Ekman balance (Figure 11b) [e.g., Kim et al., 2009]. The argument in the higher-frequency band is sensitive to the viscosity of the water column. The argument of surface currents is constant, i.e., $\pm 45^\circ$, regardless of viscosity, but in the subsurface layer (within the Ekman layer) lower viscosity causes the argument to be greater than 45° for $\omega < -f_c$ and to be less than -45° for $\omega > -f_c$ away from the inertial frequency (Figure 11d) [e.g., Gonella, 1972]. Therefore the argument difference in the seasonal transfer functions can be interpreted as reduced viscosity and more friction in summer than in winter. The viscosity is consistent with well-stratified and well-mixed upper ocean in summer and winter, respectively. However, exploring the seasonal difference in friction requires more careful analysis with numerical models.

[49] In order to facilitate quantitative comparisons of seasonal transfer functions, the ratio of magnitude (γ , \log_{10}

scale) and the argument difference ($\Delta\Theta$) at each frequency bin are shown as probability density functions in Figure 12

$$\gamma(\mathbf{x}, \omega) = \log_{10} \left[\frac{|\mathbf{H}_s(\mathbf{x}, \omega)|}{|\mathbf{H}_w(\mathbf{x}, \omega)|} \right], \quad (15)$$

$$\Delta\Theta(\mathbf{x}, \omega) = \Theta_s(\mathbf{x}, \omega) - \Theta_w(\mathbf{x}, \omega). \quad (16)$$

As the ratio is plotted in the \log_{10} scale, the positive ratio indicates that the amplitude in summer is higher than that in winter. Their ratios in the subdiurnal frequency band ($|\omega| < 1$ cpd) are well determined showing the summer transfer function to be larger than in winter, but the ratio is noisy at other frequencies (Figure 12a). Considering the argument shift at the inertial frequency, the surface currents in summer rotate more with respect to the wind direction than in winter if the argument difference is positive for $\omega < -f_c$ and negative for $\omega > -f_c$ (Figure 12b). While the argument does not show a typical tendency as the seasonal dominance, the robust estimates in several frequencies (e.g., $\omega = -1$ cpd and $\omega = 0$ cpd) are made (Figure 14).

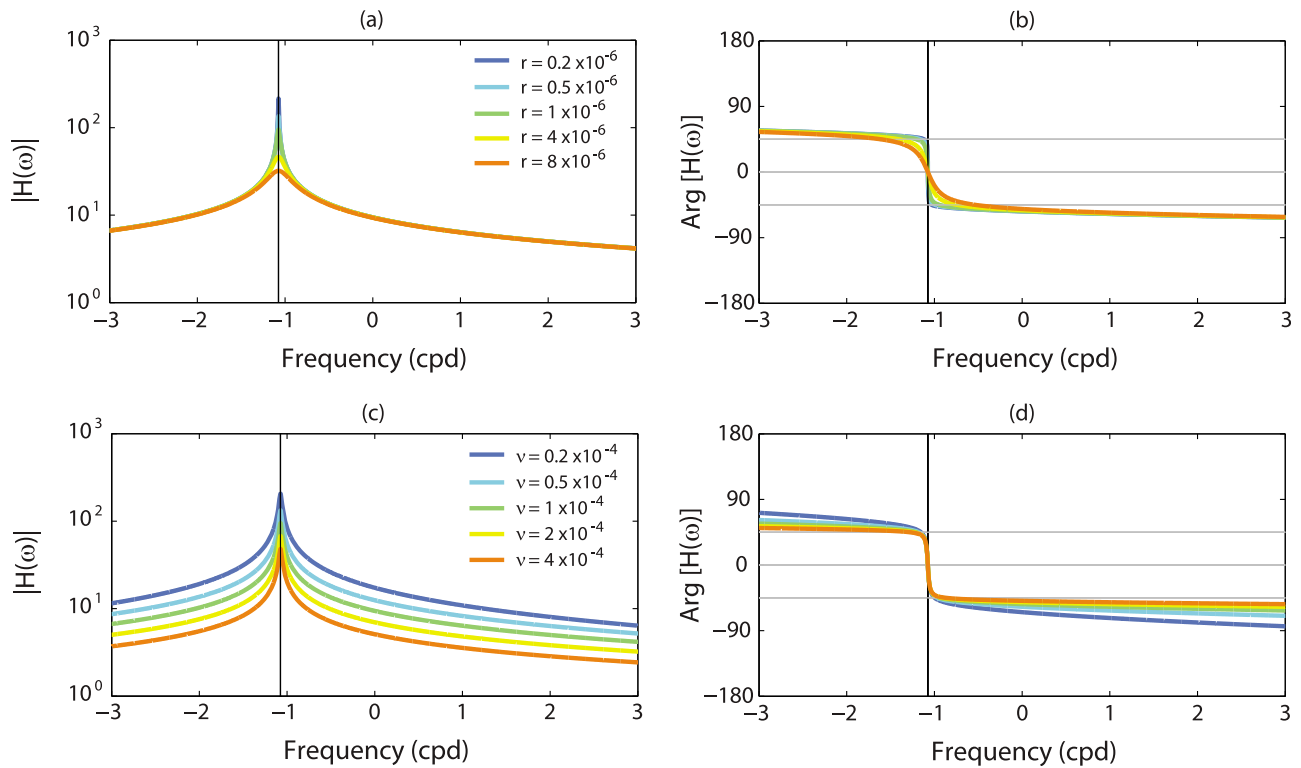


Figure 11. (a and c) Magnitude ($\text{kg}^{-1} \text{m}^2 \text{s}$) and (b and d) argument (degrees) of the isotropic transfer functions at subsurface ($z = 0.05 \delta_E$; $\delta_E = \pi\sqrt{2\nu/f_c}$ is the Ekman depth) with respect to friction (r) and viscosity (ν) are calculated from the extended Ekman model [Kim *et al.*, 2009]. Cases for varying friction and constant viscosity ($\nu = 1 \times 10^{-4} \text{m}^2 \text{s}^{-1}$, Figures 11a and 11c). Cases for varying viscosity and constant friction ($r = 1 \times 10^{-6} \text{s}^{-1}$). See Figure 5 for the gray lines.

4.4.3. Spatial Structure of Seasonal Transfer Functions

[50] In a similar way, the spatial map of seasonal transfer functions at three frequencies is presented: inertial frequency, clockwise diurnal frequency, and low frequency (Figures 13 and 14). The spatial gradient from nearshore to offshore as controlled by the surface current dynamics near the coastal boundary is similar to the full year plots.

[51] At the inertial frequency, the amplitude in summer is much stronger than in winter with negative argument in summer and positive argument in winter (Figures 13a, 13d, 14a, and 14d). As mentioned in section 4.4.1, the argument at this frequency requires careful interpretation. In the finite Fourier transform (FFT), the value at each frequency presents an averaged value over the bandwidth. Although we separate the inertial and diurnal frequencies by adjusting the FFT length, there can be a variance leakage into the nearby frequency bin. When the center of a frequency bin is located to the right of $\omega = -f_c$, the argument tends to be positive, and vice versa. Considering the sensitivity and error bar of the argument at the inertial frequency (section 4.4.1), the argument difference (Figures 14a and 14d) may be attributed as the bandwidth of diurnal wind and the current response of surface layer in the diurnal time scale (e.g., diurnal surface jet).

[52] At the diurnal frequency, the two seasonal transfer functions have nearly the same magnitude, which is not consistent with a varying thickness of the seasonal mixed layer. The argument difference is almost constant with a

range of 10° – 20° (Figures 12, 13b, 13e, 14b, and 14e). In other words, there is less rotation of narrowband diurnal winds in summer and more rotation of broadband diurnal winds in winter.

[53] In the stratified upper ocean in summer the wind and currents are expected to be more in phase than in the well-mixed water column in winter [e.g., Zhang *et al.*, 2009]. This can be considered as a current response in the shorter time scale compared to the Ekman spiral.

[54] At low frequency, the summer amplitude is stronger than in winter (Figures 13e and 13f). This can be explained by the surface layer jet with varying stratification. The same momentum supplied by the wind generates stronger but shallower currents in highly stratified water (summer) and weaker currents in the well-mixed water column (winter) (see Appendix A for more details) [e.g., Price *et al.*, 1986; Woods and Strass, 1986; Cosoli, 2006]. Other studies on wind-driven currents at and near the surface reported a larger veering angle in summer than in winter due to changes in the momentum penetration by seasonal stratification change [e.g., Schudlich and Price, 1998; Lentz, 2001; Weisberg *et al.*, 2001; Kirincich *et al.*, 2005; Dzwonkowski *et al.*, 2009; Ardhuin *et al.*, 2009; Yoshikawa and Masuda, 2009]. The veering angles of surface currents to the quasi-steady wind have means and root-mean-square (RMS) of $40.0^\circ \pm 30.5^\circ$ and $38.0^\circ \pm 22.3^\circ$ to the right of the wind direction for summer and winter, respectively. Moreover, the mean and

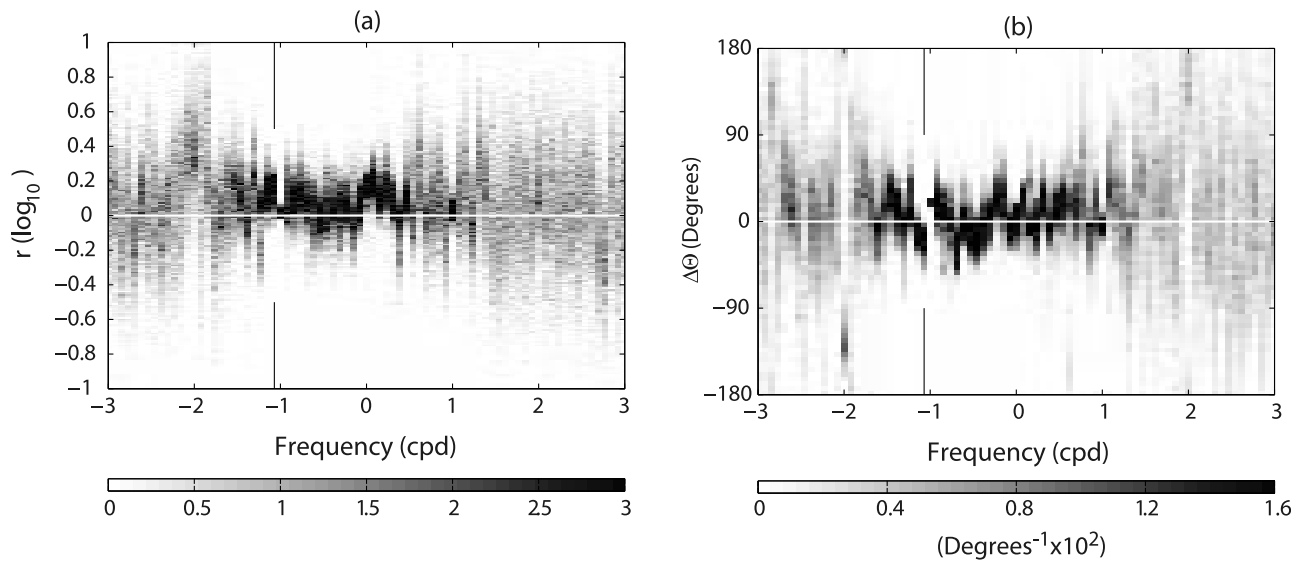


Figure 12. (a) Magnitude ratios ($\gamma(\mathbf{x}, \omega)$) and (b) argument difference ($\Delta\Theta(\mathbf{x}, \omega)$) are presented as probability density functions at each frequency bin. The ratio is on \log_{10} scale, so if the ratio is positive, the summer response is higher than the winter response. The negative argument difference means the argument in summer is more than in winter. A white horizontal line and a vertical line denote zero values and the inertial frequency, respectively.

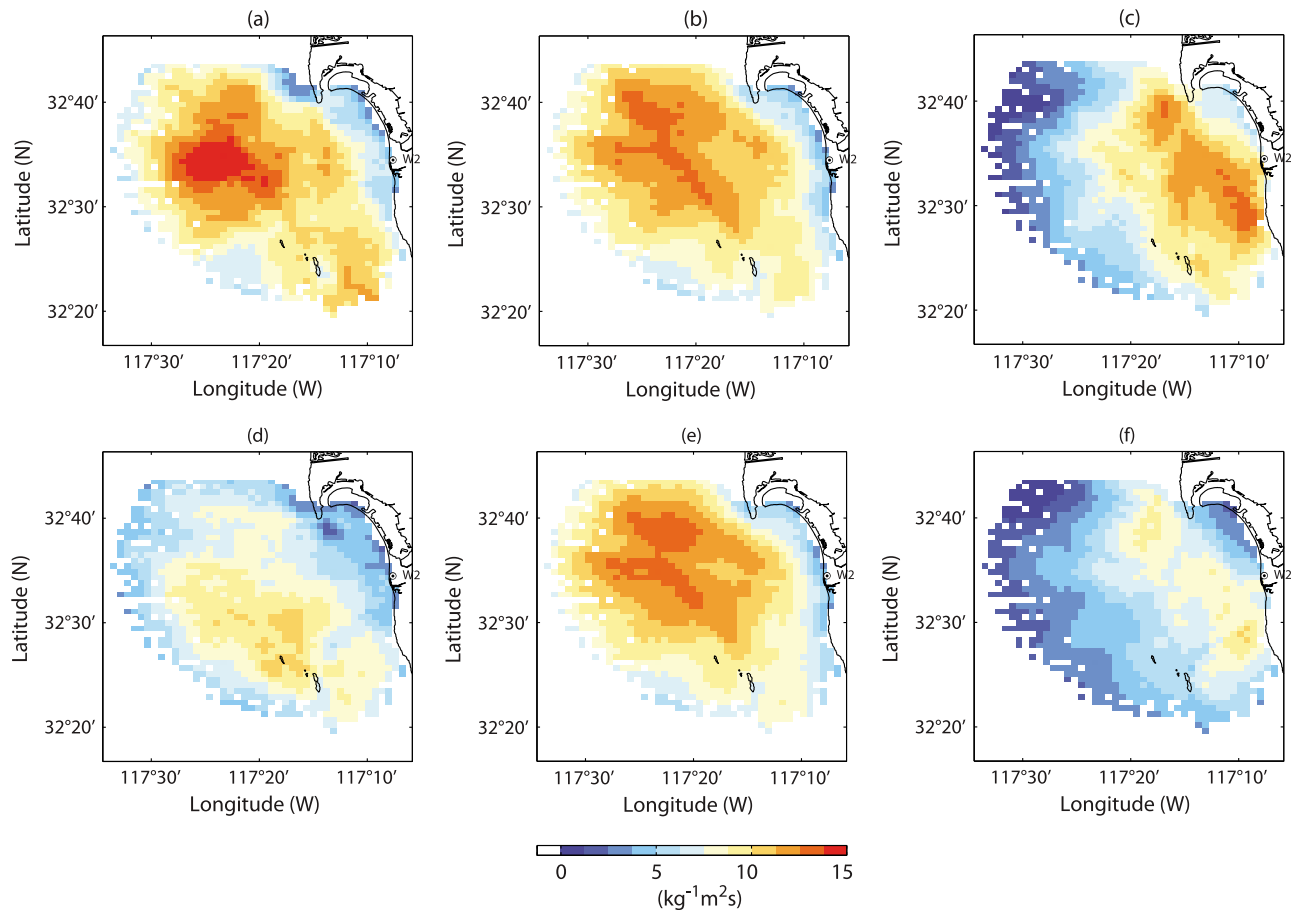


Figure 13. Magnitude ($\text{kg}^{-1} \text{m}^2 \text{s}$) of the TJR wind transfer function in (a–c) summer and (d–f) winter at (left) $\omega = -f_c$, (middle) $\omega = -1$ cpd, and (right) $\omega = 0$ cpd.

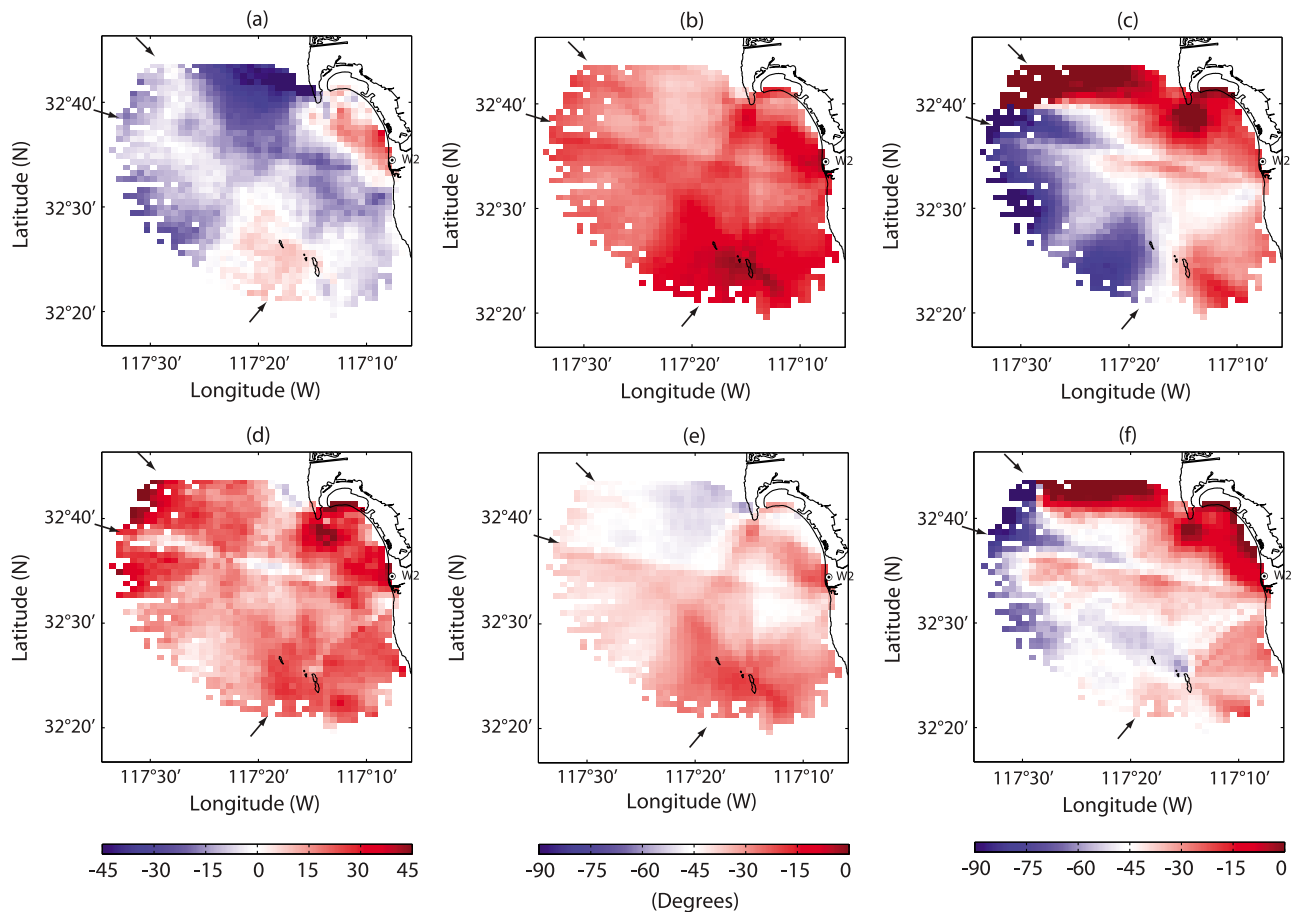


Figure 14. Argument (degrees) of the TJR wind transfer function in (a–c) summer and (d–f) winter at (left) $\omega = -f_c$, (middle) $\omega = -1$ cpd, and (right) $\omega = 0$ cpd. Three black arrows indicate the artifacts as a result of the measured beam patterns and baselines. Shared color bars are shown on the bottom.

RMS of the argument difference is $2.1^\circ \pm 30.2^\circ$. Although the averaged argument difference is not significant, the spatial influence of the stratification is more visible offshore than onshore (Figures 14c and 14f).

4.4.4. Wind Skill Mmaps

[55] The wind skill maps in summer and winter show weak differences (Figure 15). The variance of the TJR wind in winter is higher than in summer, and the TJR transfer function varies in an opposite manner. So the explained current variances are nearly the same in both seasons. For example, storm events off San Diego during winter are likely to force strong wind-driven currents. The difference in the skill map is consistent with this conjecture. The skill in summer is concentrated near the wind station, but the skill in winter is distributed broadly in the nearshore area.

5. Discussion and Conclusion

[56] We examine the wind transfer function (frequency domain) and impulse response function (time domain) using a statistical regression of wind on high-frequency radar-derived surface currents off southern San Diego. Several wind observations are used in the regression, and their contributions on wind-driven surface currents are evaluated individually and together.

[57] Transfer functions for individual wind stations (SIO, TJR, and NDBC) are consistent with a compensating scale in magnitude to reflect the relevance of offshore and nearshore winds on surface currents in a coastal region. The influence of the coast appears in their spatial structure. Transfer functions near the coast have lower amplitude at diurnal and inertial frequencies due to the circular water motion limited by the coast and higher amplitude at low frequency due to the balance of wind-driven local pressure setup at the coast and alongshore currents. The spatial gradient of the argument may result from the spatial balance between pressure setups aligned and normal to the wind and currents.

[58] In addition, the conducted analysis using independent observations in a relationship of the driving force and response reveals statistical and dynamical inconsistency and instrument errors. For example, the argument appears to be more sensitive to the radar configuration by showing the footprints of the beam pattern and baselines. In the anisotropic transfer functions (not shown), the cross-shore current response to the alongshore wind is much less than the realistic numerical model result due to relatively weak SNR of alongshore wind off southern San Diego.

[59] The impulse response function allowing for anisotropic response has been estimated considering the effective

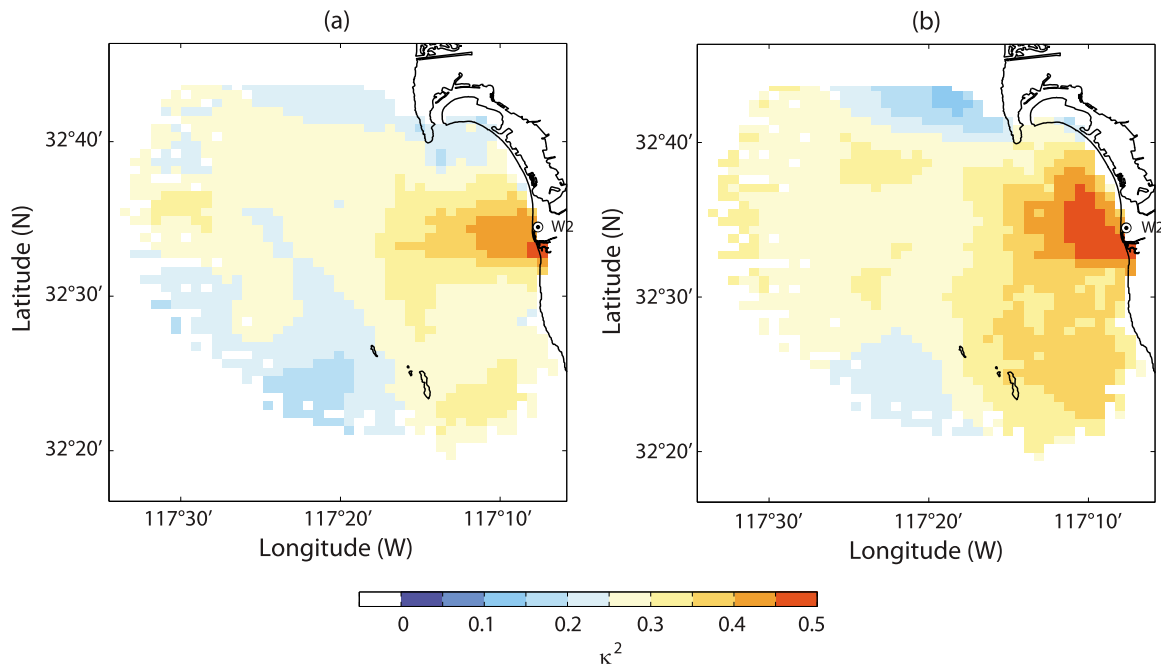


Figure 15. Wind skill map (κ^2) in (a) summer and (b) winter for frequencies at and below 2 cpd ($|\omega| \leq 2$ cpd).

inertial decay of temporal amplitude, i.e., 6 days in this region. The mean locally wind-driven surface currents are computed from two shore station winds (SIO and TJR) and the derived response function. Their magnitudes are typically 3–5% of the wind speed and the veering angles vary 50°–90° to the right of the wind at zero time lag. The time mean wind-driven surface currents show more variance nearshore than offshore, which is a similar spatial structure of the amplitude of transfer function at low frequency.

[60] The wind impulse response function and transfer function can be used to investigate the spectral content of the wind-forced currents and to derive other applications (e.g., nowcast and forecast wind-driven current estimates, and upwelling index). As a part of the statistical analysis of observed winds and surface currents, we introduce a wind skill map, which provides the variance ratio of surface currents explained by wind. The decreasing skill with distance from the wind station is attributed to the spatial decorrelation of coastal winds. As multiple wind stations are added to the regression basis, the skill becomes saturated if an appropriate regularization is applied. This wind skill map is proposed as an analysis tool to examine the data quality tool and optimal sampling of the wind and surface currents in the observations and numerical models.

[61] The seasonal difference in the wind-ocean response is considered with seasonally computed wind transfer functions. The ratios of their amplitudes in the subdiurnal frequency band are well determined and larger in summer. During summer, the magnitude of the transfer function is higher as opposed to the influence of the deeper mixed layer that results in a smaller transfer function in winter. However, the amplitudes of transfer functions at $\omega = -1$ cpd have weak seasonality. Although the difference of seasonal arguments do not have a clear contrast, the slope of the argument at the

inertial frequency and the convergence of the argument in the higher-frequency band may indicate less viscosity in summer than in winter.

[62] Analytical and numerical models will aid in understanding the dynamics such as the momentum balance between local pressure setup and currents associated with the anisotropic current response reported in this paper. Not only the current response to upwelling and downwelling favorable winds but detailed dynamic explanations in other frequency bands may be documented. Observational efforts, especially on the cross-shore structure of coastal winds [e.g., *Dorman, 1982*] can help to clarify the uncertainty and ambiguity in the spatial correlation of wind and surface currents and to study the land/sea breeze cell and the coastal marine boundary layer.

Appendix A: Stokes Drift and Surface Layer Jet

A1. Stokes Drift

[63] The contribution of the Stokes drift [e.g., *Kenyon, 1969*] to the observed surface currents is calculated as

$$\mathbf{u}_{\text{Stokes}}(z) = \frac{1}{\rho} \iint_{\mathbf{k}} E(\mathbf{k}) \frac{\mathbf{k}}{\omega} \left[\frac{2k \cosh 2k(z+h)}{\sinh 2kh} \right] d\mathbf{k}, \quad (\text{A1})$$

where $E(\mathbf{k}) = E(k, \theta) = S(k)D(\theta)$ is the surface gravity wave spectrum, which is assumed as the product of the ocean surface wave spectrum (S) and the directional distribution function (D). \mathbf{k} denotes the wave number and θ is the direction of wave relative to wind [$\mathbf{k} = (k \cos \theta, k \sin \theta)$].

[64] The directional wave spectra off San Diego are retrieved using the Maximum Entropy method [e.g., *Lygre and Korgstad, 1986; Brissette and Tsanis, 1994*] using the Coastal Data Information Program (CDIP) wave buoy

observation (Point La Jolla, 093 station). The estimated Stokes drift ranges between 2–3.5 cm s⁻¹ at the surface decreasing and about 1 cm s⁻¹ at 1 m depth. The integration interval of the wave number is between 0.004 and 1.3552 m⁻¹, which corresponds to surface waves with 0.74–250 m wavelength (or periods of 0.7–12.7 seconds). The RMS of the Stokes drift is lower than the uncertainty of HFR observations, but the Stokes drift can have a large-scale structure, if it was coherent with the winds, might affect the transfer function estimates. Even if the Stokes drift was perfectly be correlated with local winds on time scales of a few days ($|\omega| \leq 0.4$ cpd), the standard deviation of surface currents in that frequency band is 11.4 cm s⁻¹, so as a fraction of the variance, the Stokes drift is not significant.

A2. Surface Layer Jet

[65] The surface current response to the wind may vary due to changes in the upper layer stratification. The magnitude of the surface layer jet, for simplicity, depends on the mixing layer (i.e., trapping depth, D_T) that the momentum penetrates, heat flux (Q), and wind stress (τ) [e.g., Phillips, 1966; Price *et al.*, 1986; Woods and Strass, 1986]

$$|\mathbf{u}| \propto \frac{\tau}{D_T} \quad \text{and} \quad D_T \propto \frac{\tau}{\sqrt{Q}}. \quad (\text{A2})$$

The seasonal and daily surface layer jets are explored with the Price-Weller-Pinkel (PWP) model [Price *et al.*, 1986] using seasonal/daily heat flux and wind stress in southern San Diego. The data are from the NCEP/NCAR heat flux reanalysis data [Kalnay *et al.*, 1996] and two wind observations (SIO and TJR). The surface layer jet shows the vertical momentum penetration from the surface in clockwise. The order of magnitude of the surface layer jet is 2–3 cm s⁻¹, which is relatively small compared to the total variance of surface currents, because the nearshore wind stress is much weaker than offshore, and the diurnal winds within the land/sea breeze cell would not produce the current response of the same order as a steady wind stress [Price *et al.*, 1986]. Considering the seasonal variation of the wind stress and heat flux in the San Diego area, the surface layer jet can be estimated approximately. The heat flux in summer is approximately 55% higher than that in winter. However, the wind stress in winter is about 56% stronger than that in summer

$$|Q_s| = 1.55|Q_w|, \quad (\text{A3})$$

$$|\tau_w| = 1.56|\tau_s|. \quad (\text{A4})$$

[66] From equation (A2), the mixing layer in the winter is about 95% deeper than in summer and it results in 25% increase of the surface layer jet in summer

$$D_{T_w} = 1.95D_{T_s}, \quad (\text{A5})$$

$$|\mathbf{u}_s| = 1.25|\mathbf{u}_w|. \quad (\text{A6})$$

The surface layer jet is considered to be embedded partially in both locally wind-driven surface currents coupled with

seasonal stratification and heat flux and diurnal band surface currents.

Appendix B: Regression Using Multiple Basis Functions

[67] The regression using multiple basis functions is presented as a simple inverse problem [e.g., Wunsch, 1996]

$$\mathbf{Z}\mathbf{m} = \mathbf{d}, \quad (\text{B1})$$

where \mathbf{Z} , \mathbf{m} , and \mathbf{d} correspond to the matrix composed of wind data at multiple stations (τ), the transfer function (\mathbf{H}) or response function (\mathbf{G}), and the surface currents (\mathbf{u}), respectively. The estimated model coefficients ($\hat{\mathbf{m}}$) are

$$\begin{aligned} \hat{\mathbf{m}} &= \mathbf{P}\mathbf{Z}^\dagger(\mathbf{Z}\mathbf{P}\mathbf{Z}^\dagger + \mathbf{R})^{-1}\mathbf{d} \\ &= (\mathbf{Z}^\dagger\mathbf{R}^{-1}\mathbf{Z} + \mathbf{P}^{-1})^{-1}\mathbf{Z}^\dagger\mathbf{R}^{-1}\mathbf{d}, \end{aligned} \quad (\text{B2})$$

where \mathbf{P} and \mathbf{R} are the model and error covariance matrices († is the matrix transpose).

[68] In this paper, the error covariance matrix (\mathbf{R}) is assumed to be an identify matrix (\mathbf{I}) to make an equivalent form of equation (2), which indicates, in turn, the regularization matrix (\mathbf{R}_c) in equation (2) is an inverse of the model covariance matrix (\mathbf{P})

$$\mathbf{R}_c = \mathbf{P}^{-1}. \quad (\text{B3})$$

[69] This modification allows us to adjust SNR easily by changing only the matrix \mathbf{P} , which can be a scaled diagonal matrix reflecting the contribution of each wind basis function

$$\mathbf{P} = \begin{bmatrix} \alpha_1^{-2} & 0 & 0 \\ 0 & \alpha_2^{-2} & 0 \\ 0 & 0 & \alpha_3^{-2} \end{bmatrix}. \quad (\text{B4})$$

[70] **Acknowledgments.** Sung Yong Kim is supported by the Coastal Ocean Currents Monitoring Program (COCMP) from the State of California and the Office of Naval Research (ONR). Bruce Cornuelle is sponsored by both NOAA (NOAA award NA17RJ1231) and COCMP. Eric Terrill is supported through funding provided by the ONR, COCMP, and NOAA. Surface current data are provided from the Southern California Coastal Ocean Observing System (SCCOOS), available online at <http://www.sccoos.org> at Scripps Institution of Oceanography (SIO). Wind data at the Tijuana River (Tidal Linkage) are maintained by the System-Wide Monitoring Program at the Tijuana River National Estuarine Research Reserve, Estuarine Reserves Division (TRNERR), NOAA, Centralized Data Management Office (CDMO), Baruch Marine Field Lab, and University of South Carolina. Wind data at the SIO Pier are maintained by the Integrative Oceanography Division (IOD) and the wind at the NDBC buoy is available online <http://www.ndbc.noaa.gov/>. CTD sampling data are provided through SCCOOS from South Bay Outfall Monitoring Program. We thank M. Otero, L. Hazard, P. Reuter, J. Bowen, and T. Cook at Coastal Observing Research and Development Center (CORDC, available online at <http://cordc.ucsd.edu>) at SIO and M. Ide, M. Cordrey, and J. Crook in TRNERR.

References

Allen, J. S. (1980), Models of wind-driven currents on the continental shelf, *Annu. Rev. Fluid Mech.*, 12, 389–433.

- Almeida, F. M. S. C. (2008), The influence of wind on HF radar surface current forecasts, M.S. thesis, Nav. Postgrad. Sch., Monterey, Calif.
- Ardhuin, F., L. Marié, N. Rascle, P. Forget, and A. Roland (2009), Observation and estimation of Lagrangian, Stokes, and Eulerian currents induced by wind and waves at the sea surface, *J. Phys. Oceanogr.*, *39*, 2820–2838, doi:10.1175/2009JPO4169.1.
- Atkinson, B. W. (1981), *Meso-Scale Atmospheric Circulation*, 496 pp., Academic, London.
- Beardsley, R. C., C. E. Dorman, C. A. Friehe, L. K. Rosenfeld, and C. D. Winant (1987), Local atmospheric forcing during the Coastal Ocean Dynamics Experiment: 1. A description of the marine boundary layer and atmospheric conditions over a northern California upwelling region, *J. Geophys. Res.*, *92*(C2), 1467–1488.
- Bendat, J. S., and A. G. Piersol (2000), *Random Data: Analysis and Measurement Procedures*, 3rd ed., 594 pp., John Wiley, New York.
- Bretherton, C. S., M. Widmann, V. P. Dymnikov, J. M. Wallace, and I. Bladé (1999), The effective number of spatial degrees of freedom of a time-varying field, *J. Clim.*, *12*(7), 1990–2009.
- Brissette, F. P., and I. K. Tsanis (1994), Estimation of wave directional spectra from pitch-roll buoy data, *J. Waterw. Port Coastal Ocean Eng.*, *120*, 93–115.
- Bye, J. A. T. (1965), Wind-driven circulation in unstratified lakes, *Limnol. Oceanogr.*, *10*, 451–458.
- Churchill, G. H., and G. T. Csanady (1983), Near-surface measurements of quasi-Lagrangian velocities in open water, *J. Phys. Oceanogr.*, *13*, 1669–1680.
- Constable, S. C., R. L. Parker, and C. G. Constable (1987), Ocean's inversion: A practical algorithm for generating smooth models from electromagnetic sounding data, *Geophysics*, *52*(3), 289–300.
- Cosoli, S. (2006), Interference of the three-dimensional flow field in shallow water environments: Application of the “velocity projection technique” to the northern Adriatic Sea, Ph.D. thesis, Univ. Ca’Foscari di Venezia, Venice, Italy.
- Cronin, M. F., and W. S. Kessler (2008), Near-surface shear flow in the tropical Pacific cold tongue front, *J. Phys. Oceanogr.*, *39*, 1200–1215, doi:10.1175/2008JPO4064.1.
- Csanady, G. T. (1982), *Circulation in the Coastal Ocean*, 279 pp., D. Reidel, Dordrecht, Netherlands.
- D’Asaro, E. A. (1985), The energy flux from the wind to the near-inertial motions in the surface mixed layer, *J. Phys. Oceanogr.*, *15*, 1043–1059.
- Davies, A. M. (2003), On the interaction between internal tides and wind-induced near-inertial currents at the shelf edge, *J. Geophys. Res.*, *108*(C3), 3099, doi:10.1029/2002JC001375.
- Davis, R. E. (1985), Objective mapping by least squares fitting, *J. Geophys. Res.*, *90*(C7), 4773–4777.
- Davis, R. E., R. deSzoeke, and P. Niiler (1981), Variability in the upper ocean during MILE. Part II: modeling the mixed layer response, *Deep Sea Res. Part A*, *28*, 1453–1475, doi:10.1016/0198-0149(81)90092-3.
- Dorman, C. E. (1982), Winds between San Diego and San Clemente Island, *J. Geophys. Res.*, *87*(C12), 9636–9646.
- Dorman, C. E., and C. D. Winant (1995), Buoy observations of the atmosphere along the West Coast of the United States, 1981–1990, *J. Geophys. Res.*, *100*(C8), 16,029–16,044.
- Dzwonkowski, B., J. T. Kohut, and X.-H. Yan (2009), Seasonal difference in wind-driven across-shelf forcing and response relationships in the shelf surface layer of the central Mid-Atlantic Bight, *J. Geophys. Res.*, *114*, C08018, doi:10.1029/2008JC004888.
- Efron, B., and G. Gong (1983), A leisurely look at the bootstrap, the Jackknife, and the cross-validation, *Am. Stat.*, *37*(1), 36–48.
- Ekman, V. W. (1905), On the influence of the Earth’s rotation on ocean currents, *Ark. Mat. Astron. Fys.*, *2*, 1–53.
- Elipot, S. (2006), Spectral characterization of Ekman velocities in the Southern Ocean based on surface drifter trajectories, Ph.D. thesis, Scripps Inst. of Oceanogr., Univ. of Calif. San Diego, La Jolla, Calif. (Available at <http://escholarship.org/uc/item/1ks7v6wm>.)
- Essen, H.-H. (1993), Ekman portion of surface currents as measured by radar in different areas, *Dtsch. Hydrogr. Z.*, *45*(2), 57–85.
- Estoque, M. A. (1961), A theoretical investigation of the sea breeze, *Q. J. R. Meteorol. Soc.*, *87*, 136–140, doi:10.1002/qj.49708737203.
- Fernandez, D. M., J. F. Veseky, and C. C. Teague (1996), Measurements of upper ocean surface current shear with high-frequency radar, *J. Geophys. Res.*, *101*(C12), 28,615–28,625.
- Garratt, J. R. (1977), Review of drag coefficients over oceans and continents, *Mon. Weather Rev.*, *105*, 915–929.
- Gonella, J. (1971), A local study of inertial oscillation in the upper layers of the ocean, *Deep Sea Res. Oceanogr. Abstr.*, *18*, 775–788.
- Gonella, J. (1972), A rotary-component method for analysis in meteorological and oceanographic vector time series, *Deep Sea Res. Oceanogr. Abstr.*, *19*, 833–846.
- Graber, H. C., B. K. Haus, R. D. Chapman, and L. K. Shay (1997), HF radar comparisons with moored estimates of current speed and direction: Expected differences and implications, *J. Geophys. Res.*, *102*(C8), 18,749–18,766.
- Hodur, R. M. (1997), The Naval Research Laboratory’s Coupled Ocean/Atmosphere Mesoscale Prediction System (COAMPS), *Mon. Weather Rev.*, *125*, 1414–1430.
- Inman, J. R. (1975), Resistivity inversion with ridge regression, *Geophysics*, *40*(5), 798–817.
- Kalnay, E., et al. (1996), The NCEP/NCAR 40-year reanalysis project, *Bull. Am. Meteorol. Soc.*, *77*(3), 437–471.
- Kenyon, K. K. (1969), Stokes drift for random gravity waves, *J. Geophys. Res.*, *74*(28), 6691–6694.
- Kim, S. Y. (2010), Observations of submesoscale eddies using high-frequency radar-derived kinematic and dynamic quantities, *Cont. Shelf Res.*, *30*, 1639–1655, doi:10.1016/j.csr.2010.06.011.
- Kim, S. Y., E. J. Terrill, and B. D. Cornuelle (2007), Objectively mapping HF radar-derived surface current data using measured and idealized data covariance matrices, *J. Geophys. Res.*, *112*, C06021, doi:10.1029/2006JC003756.
- Kim, S. Y., E. J. Terrill, and B. D. Cornuelle (2008), Mapping surface currents from HF radar radial velocity measurements using optimal interpolation, *J. Geophys. Res.*, *113*, C10023, doi:10.1029/2007JC004244.
- Kim, S. Y., B. D. Cornuelle, and E. J. Terrill (2009), Anisotropic response of surface currents to the wind in a coastal region, *J. Phys. Oceanogr.*, *39*, 1512–1533, doi:10.1175/2009JPO4013.1.
- Kim, S. Y., B. D. Cornuelle, and E. J. Terrill (2010), Decomposing observations of high-frequency radar-derived surface currents by their forcing mechanisms: Decomposition techniques and spatial structures of decomposed surface currents, *J. Geophys. Res.*, *115*, C12007, doi:10.1029/2010JC006222.
- Kirincich, A. R., J. A. Barth, B. A. Grantham, B. A. Menge, and J. Lubchenco (2005), Wind-driven inner-shelf circulation off central Oregon during summer, *J. Geophys. Res.*, *110*, C10S03, doi:10.1029/2004JC002611.
- Kudryavtsev, V., V. Shrira, V. Dulov, and V. Malinovsky (2008), On the vertical structure of wind-driven sea currents, *J. Phys. Oceanogr.*, *38*, 2121–2144, doi:10.1175/2008JPO3883.1.
- Lanczos, C. (1956), *Applied Analysis*, 539 pp., Prentice-Hall, Eaglewood Cliffs, N. J.
- Large, W. G., and S. Pond (1981), Open ocean momentum flux measurements in moderate to strong winds, *J. Phys. Oceanogr.*, *11*, 324–336.
- Large, W. G., J. Morzel, and G. B. Crawford (1995), Accounting for surface wave distortion of the marine wind profile in low-level ocean storms wind measurements, *J. Phys. Oceanogr.*, *25*, 2959–2971.
- Laws, K. (2001), Measurements of near surface ocean currents using HF radar, Ph.D. thesis, Univ. of Calif. Santa Cruz, Santa Cruz, Calif.
- LeBlanc, M., and R. Tibshirani (1996), Combining estimates in regression and classification, *J. Am. Stat. Assoc.*, *91*(436), 1641–1650.
- Lentz, S. J. (2001), The influence of stratification on the wind-driven cross-shelf circulation over the north Carolina shelf, *J. Phys. Oceanogr.*, *31*, 2749–2760.
- Li, Z., and R. H. Weisberg (1999), West Florida shelf response to upwelling favorable wind forcing: Kinematics, *J. Geophys. Res.*, *104*(C6), 13,507–13,527.
- Lygre, A., and H. E. Korgstad (1986), Maximum entropy estimation of the directional distribution in ocean wave spectra, *J. Phys. Oceanogr.*, *16*, 2052–2060.
- Madsen, O. S. (1977), A realistic model of the wind-induced Ekman boundary layer, *J. Phys. Oceanogr.*, *7*, 248–255.
- Mao, Y., and M. L. Heron (2008), The influence of fetch on the response of surface currents to wind studied by HF ocean surface radar, *J. Phys. Oceanogr.*, *38*, 1107–1121, doi:10.1175/2007JPO3709.1.
- Ng, B. (1993), The prediction of nearshore wind-induced surface currents from wind velocities measured at nearby land stations, *J. Phys. Oceanogr.*, *23*, 1609–1617.
- Pawlowicz, R., B. Beardsley, and S. Lentz (2002), Classic tidal harmonic analysis including error estimates in MATLAB using T_TIDE, *Comput. Geosci.*, *28*, 929–937.
- Perlin, A., J. N. Moum, and J. M. Klymak (2005), Response of the bottom boundary layer over a sloping shelf to variations in alongshore wind, *J. Geophys. Res.*, *110*, C10S09, doi:10.1029/2004JC002500.
- Perlin, A., J. N. Moum, J. M. Klymak, M. D. Levine, T. Boyd, and P. M. Kosro (2007), Organization of stratification, turbulence, and veering in bottom Ekman layers, *J. Geophys. Res.*, *112*, C05S90, doi:10.1029/2004JC002641.
- Phillips, O. M. (1966), *The Dynamics of the Upper Ocean*, 336 pp., Cambridge Univ. Press, Cambridge, U. K.

- Pidgeon, E. J., and C. D. Winant (2005), Diurnal variability in currents and temperature on the continental shelf between central and southern California, *J. Geophys. Res.*, *110*, C03024, doi:10.1029/2004JC002321.
- Pollard, R. T., and R. C. Millard Jr. (1970), Comparison between observed and simulated wind-generated inertial oscillations, *Deep Sea Res. Oceanogr. Abstr.*, *17*, 813–821.
- Ponte, A. L. S. (2010), Periodic wind-driven circulation in an elongated and rotating basin, *J. Phys. Oceanogr.*, *40*, 2043–2058, doi:10.1175/2010JPO4235.1.
- Prandle, D. (1987), The fine-structure of nearshore tidal and residual circulations revealed by HF radar surface current measurements, *J. Phys. Oceanogr.*, *17*, 231–245.
- Price, J. F., R. A. Weller, and R. Pinkel (1986), Diurnal cycling: Observations and models of the upper ocean response to diurnal heating, cooling, and wind mixing, *J. Geophys. Res.*, *91*(C7), 8411–8427.
- Priestley, M. B. (1981), *Spectral Analysis and Time Series*, 890 pp., Academic, London.
- Rabinovich, A. B., G. V. Shevchenko, and R. E. Thomson (2007), Sea ice and current response to the wind: A vector regression analysis approach, *J. Atmos. Oceanic Technol.*, *24*, 1086–1101, doi:10.1175/JTECH2015.1.
- Rio, M.-H., and F. Hernandez (2003), High-frequency response of wind-driven currents measured by drifting buoy and altimetry over the world ocean, *J. Geophys. Res.*, *108*(C8), 3283, doi:10.1029/2002JC001655.
- Ryan, H. F., and M. A. Noble (2006), Alongshore wind forcing of coastal sea level as a function of frequency, *J. Phys. Oceanogr.*, *36*, 2173–2184.
- Schudlich, R. R., and J. F. Price (1998), Observations of seasonal variation in the Ekman layer, *J. Phys. Oceanogr.*, *28*, 1187–1204.
- Spaulding, M. (1999), Drift current under the action of wind and waves, in *Wind-Over-Wave Couplings*, edited by S. G. Sajjadi, N. H. Thomas, and J. C. R. Hunt, pp. 243–256, Clarendon, Oxford, U. K.
- Tikhonov, A. N., and V. Y. Arsenin (1977), *Solutions of Ill-Posed Problems*, 258 pp., Halsted, Winston, Wash.
- Ullman, D. S., J. O'Donnell, J. Kohut, T. Fake, and A. Allen (2006), Trajectory prediction using HF radar surface currents: Monte Carlo simulations of prediction uncertainties, *J. Geophys. Res.*, *111*, C12005, doi:10.1029/2006JC003715.
- von Storch, H., and F. Zwiers (1999), *Statistical Analysis in Climate Research*, 484 pp., Cambridge Univ. Press, Cambridge, U. K.
- Weber, J. E. (1983), Steady wind- and wave-induced currents in the open ocean, *J. Phys. Oceanogr.*, *13*, 524–530.
- Weisberg, R., and L. Pietrafesa (1983), Kinematics and correlation of the surface wind field in the South Atlantic Bight, *J. Geophys. Res.*, *88*(C8), 4593–4610.
- Weisberg, R. H., Z. Li, and R. Muller-Karger (2001), West Florida shelf response to local wind forcing: April 1998, *J. Geophys. Res.*, *106*(C12), 31,239–31,262.
- Weller, R. A. (1981), Observations of the velocity response to wind forcing in the upper ocean, *J. Geophys. Res.*, *86*(C3), 1969–1977.
- Winant, C. D. (2004), Three-dimensional wind-driven flow in an elongated rotating basin, *J. Phys. Oceanogr.*, *34*, 462–476.
- Woods, J. D., and V. Strass (1986), The response of the upper ocean to solar heating II: The wind-driven current, *Q. J. R. Meteorol. Soc.*, *112*, 29–42.
- Wu, J. (1983), Sea-surface drift currents induced by wind and waves, *J. Phys. Oceanogr.*, *13*, 1441–1451.
- Wunsch, C. (1996), *The Ocean Circulation Inverse Problem*, 442 pp., Cambridge Univ. Press, Cambridge, U. K.
- Yelland, M., and P. K. Taylor (1996), Wind stress measurements from the open ocean, *J. Phys. Oceanogr.*, *26*, 541–558.
- Yoshikawa, Y., and A. Masuda (2009), Seasonal variations in the speed factor and deflection angle of the wind-driven surface flow in the Tsushima Strait, *J. Geophys. Res.*, *114*, C12022, doi:10.1029/2009JC005632.
- Zhang, X., S. F. DiMarco, D. C. Smith, M. K. Howard, A. E. Jochens, and R. D. Hetland (2009), Near-resonant ocean response to sea breeze on a stratified continental shelf, *J. Phys. Oceanogr.*, *39*, 2137–2155, doi:10.1175/2009JPO4054.1.

B. D. Cornuelle, Climate, Atmospheric Science and Physical Oceanography, Scripps Institution of Oceanography, University of California, San Diego, 9500 Gilman Dr., La Jolla, CA 92093, USA.

S. Y. Kim and E. J. Terrill, Marine Physical Laboratory, Scripps Institution of Oceanography, University of California, San Diego, 9500 Gilman Dr., La Jolla, CA 92093, USA. (syongkim@mpl.ucsd.edu)